Near-field modeling of the 1964 Alaska tsunami: the role of splay faults and horizontal displacements

Elena Suleimani[1] **and Jeffrey T. Freymueller**[1,2]

[1]Geophysical Institute, University of Alaska Fairbanks, Fairbanks, Alaska, USA
[2]Now at Dept. of Earth and Environmental Sciences, Michigan State University, East Lansing, Michigan, USA

Key Points:

- Secondary splay faults and horizontal displacements played an important role in generating destructive tsunami waves during the 1964 earthquake.
- Splay faults ruptured offshore beyond their mapped dimensions on land.
- A newly modified coseismic deformation model provides a good estimate of tsunami first arrivals at Kodiak island.

Corresponding author: Elena Suleimani, ensuleimani@alaska.edu

Abstract

Near-field observations of tsunami waves generated by the M_{W}9.2 1964 Alaska earthquake reveal a complex relationship between coseismic slip and the tsunami wavefield in the source area. The documented times and amplitudes of first arrivals, measured runup heights and inundation areas along the coasts of the Kenai Peninsula and Kodiak Island show that secondary splay faults played an important role in generating destructive tsunami waves. We find that a splay fault extending to about 150°W is required to fit tsunami first arrivals on the Kenai Peninsula, but that the splay fault did not rupture along the entire length of the Kenai Peninsula. This extent supports the connection of splay faulting to a persistent Prince William Sound asperity. Our results also show that the contribution of coseismic horizontal displacements into the initial tsunami wave field does not change the pattern of tsunami arrivals much, but increases the amplitude. The coseismic deformation model of Suito and Freymueller (2009) explains the pattern of tsunami arrivals in the Kodiak Island region well, indicating that it provides a good estimate of slip on the megathrust in the Kodiak asperity. The sensitivity of the near-field arrival information to the coseismic slip model shows that such data are important in distinguishing between slip on splay faults and on the megathrust, and in discriminating between competing slip models.

1 Introduction

The Great Alaska Earthquake of March 27, 1964 generated the most destructive tsunami ever observed in North America. The major tectonic tsunami, which was produced by displacement of the ocean floor between the trench and the coastline, caused fatalities and great damage in Alaska, Hawaii, and the west coast of the United States and Canada (Spaeth & Berkman, 1972). Of the 131 fatalities associated with this earthquake, 122 were caused by tsunami waves (Lander, 1996). The earthquake ruptured an 800-km long section of the Aleutian megathrust (Figure 1, inset), producing vertical displacements over an area of about 285,000 km^2 in south-central Alaska (Plafker, 1969). The area of coseismic subsidence included parts of Kodiak Island, Kenai Peninsula, Cook Inlet and Prince William Sound, with the axis of maximum subsidence approximately along the downdip end of the rupture zone (Figure 1, inset). The major zone of coseismic uplift was seaward of the subsidence zone, in Prince William Sound and in the Gulf of Alaska (Plafker, 1969). In addition to the tectonic tsunami waves, more than twenty local tsunamis were generated by submarine and subaerial landslides in coastal Alaska.

The rupture area of the 1964 earthquake is at the eastern end of the Aleutian Megathrust (Figure 1). This subduction zone has a history of producing large and great earthquakes (1938, 1946, 1957, 1964 and 1965) and generating both local and Pacific-wide tsunamis (Lander, 1996). Nishenko and Jacob (1990) compiled a record of past large and great earthquakes along the Pacific/North American plate boundary, using historical, instrumental, and paleoseismic observations. They defined segments of the Aleutian megathrust as subduction zone sections that have been repeatedly ruptured by large and great earthquakes, or as gaps between rupture segments. According to this model, south-central Alaska includes two segments of the megathrust that ruptured in 1964: Prince William Sound (PWS), and Kodiak Island (KI), and one that did not: Yakataga-Yakutat (YY) (Figure 1, inset). The PWS and KI segments have different pre-1964 earthquake histories. The KI segment has produced large and great earthquakes independently of the PWS segment, with the recurrence interval for the Kodiak asperity estimated as low as 60 years, while that for the PWS asperity appears to be several centuries (Nishenko & Jacob, 1990). Carver and Plafker (2008) recognized nine paleosubduction earthquakes in the PWS segment in the past ∼5000 years from paleoseismic evidence of sudden land changes and tsunami deposits in the Copper River Delta in the eastern part of the Aleutian megathrust.

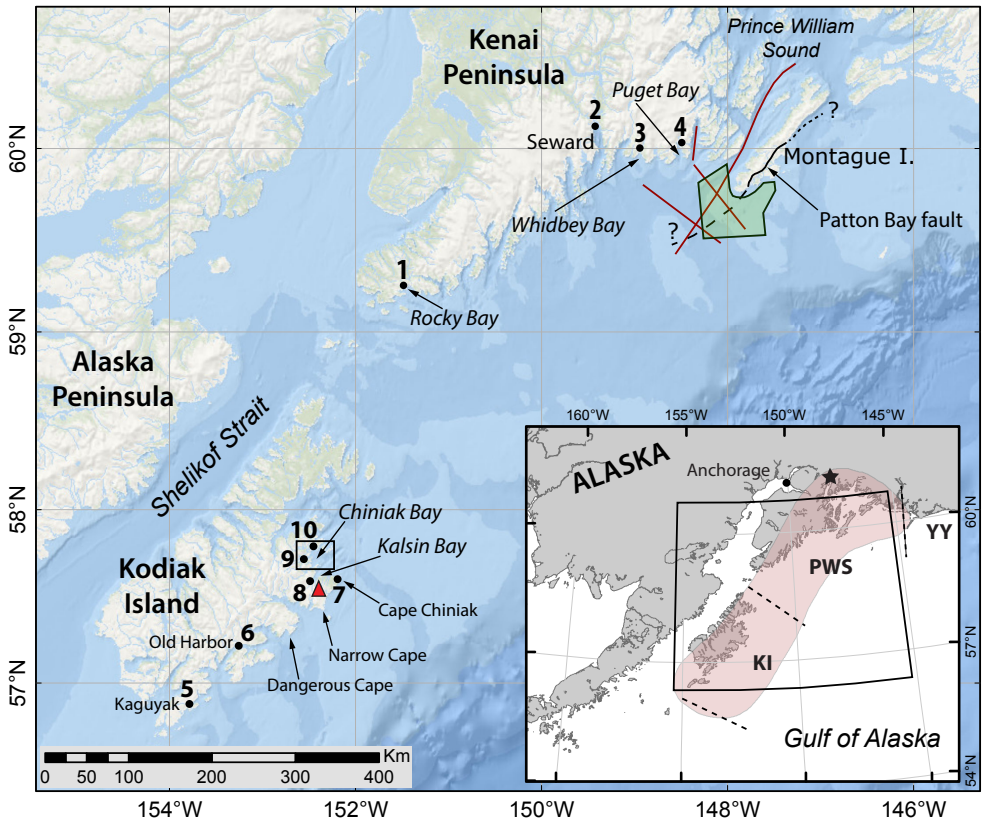

Figure 1. Map of south-central Alaska with the rupture zone of the M_w9.2 1964 Great Alaska earthquake. In the inset map, the star indicates the earthquake epicenter, the pink region delineates the 1964 rupture area (Plafker, 1969); KI - Kodak Island, PWS - Prince William Sound, and YY - Yakataga-Yakutat segments. The Patton Bay fault is shown by solid, dashed and dotted lines where it is mapped, approximated and inferred, respectively. Numbers indicate locations of time series points listed in Table 1. The red triangle next to Kalsin Bay shows the location of the USGS streamflow gauge that recorded tsunami waves. The green shaded polygon southwest of Montague Island outlines the area of the 1965 marine geophysical survey performed by ship "Surveyor" (Malloy & Merrill, 1972). Red lines are locations of seismic profiles described in Liberty et al. (2013).

Table 1. Compilation of tsunami observations collected after the 1964 earthquake in the Gulf of Alaska. The locations listed in the table are shown in Figure 1.

No.	Location	Arrival (min)	First motion	Crest height (m)	Runup (m)	Source of data
1	Rocky Bay	30 (?)	down	about 2.7 m	6	Plafker et al. (1969)
2	Seward	35	up	6-8 m	9.5	Wilson and Tørum (1968); Lemke (1967)
3	Whidbey Bay	19.5 ± 0.5	up		10.5	Plafker et al. (1969)
4	Puget Bay	20 ± 2	up		8.5	Plafker et al. (1969)
5	Kaguyak	20	up	4.6	5	Wilson and Tørum (1968); Plafker and Kachadoorian (1966)
6	Old Harbor	48	up		3.7	Plafker and Kachadoorian (1966)
7	Cape Chiniak	38	up	9		Plafker and Kachadoorian (1966)
8	Kalsin Bay	70			4.6	Plafker and Kachadoorian (1966)
9	Kodiak Naval Station	63	up	3.5		Kachadoorian and Plafker (1969)
10	Kodiak City	45(?)	up	6	8	Wilson and Tørum (1968); Kachadoorian and Plafker (1969)

The slip distribution in the 1964 rupture included a substantial amount of slip on intraplate splay faults, resulting in up to 10 meters of surface offset on the Patton Bay fault (Plafker, 1969, 2006). The tsunami waves produced by slip on a splay fault will arrive before waves generated by slip on the megathrust; therefore the initial tsunami wave can be higher and arrive sooner if slip on a splay fault is significant. Plafker (1967) presented the most detailed description and tectonic analysis of the Patton Bay and Hanning Bay reverse faults that ruptured during the 1964 Alaska earthquake. Plafker suggested that the Patton Bay fault marks the northern end of a system of discontinuous faults that continues in the ocean floor well past where was then mapped, for additional 480 km. The 1964 rupture was traced on land for about 35 km, and also on the seafloor southwest of the Montague Island for about 27 km (Malloy and Merrill (1972); see also Figure 1). However, it was not clear from those earlier studies how far offshore the 1964 splay fault ruptures extended. More recently, Liberty et al. (2013) examined the fault offsets on splay faults west of Montague Island based on high frequency seismic reflection data (Figure 1), and found that several splay faults had accumulated significant slip over the Holocene. Liberty et al. (2019) showed that repeated ruptures of a set of splay faults had occurred along with past megathrust earthquakes, with a similar slip pattern as in 1964. They concluded that the extent of rupture on the splay faults was linked to the along-strike limits of the PWS asperity, and that the asperity had been persistent over many earthquake cycles.

Other tsunami generation mechanisms can also be responsible for discrepancies between observed tsunami amplitudes and modeling results. The arrivals of tectonic waves inside of Prince William Sound were masked by large locally landslide-generated waves in Valdez and Whittier (Coulter & Migliaccio, 1966; Kachadoorian, 1965). Based on analysis of the seismically-inverted sea floor deformation of the 2004 Sumatra-Andaman earthquake, Song et al. (2008) concluded that a significant portion of the total tsunami energy was due to the horizontal displacements of the seafloor. Since the geometry of the 1964 rupture was similar to that of the Sumatra earthquake, and large coseismic horizontal displacements were observed, it is reasonable to assume that they had sizable contribution to tsunami generation during the Great Alaska earthquake.

This paper presents the first near-field numerical modeling study of the 1964 tsunami source mechanism, which requires good knowledge of the slip distribution in the rupture area (Suleimani et al., 2003). We focus on important features of the coseismic slip model that affect the near-field inundation modeling results, including splay faults and horizontal displacements. The next section describes the numerical tools and data that we use to simulate and analyze the effects of tsunami waves along the coasts of the Kenai Peninsula and Kodiak Island. Section 3 compares predictions for far-field and near-field tsunamis from the three most recently published slip models, and Section 4 describes the process of building an updated source function based on the fault geometry and the initial coseismic slip distribution of the most recent model of Suito and Freymueller (2009), which fits the near-field data most closely. We assess the effects of the splay fault displacements and the component of the vertical deformation of the sea surface due to horizontal displacement of the sloping seafloor in Section 4.3. This will contribute to better understanding of the tsunami threat to Alaska coast and to more efficient tsunami hazard mitigation.

2 Methodology

In this section we describe the numerical tools and data that we use to study the 1964 tsunami in the near field, including Kodiak Island and the Kenai Peninsula (Figure 1). In the near field, tsunami modeling results are extremely sensitive to the fine structure of the tsunami source, as well as the quality and resolution of the bathymetry and topography data. We use forward rather than inverse modeling of tsunami and geodetic data for the same reasons given in Suito and Freymueller (2009): the geodetic coseis-

mic displacement data suffer from systematic errors, inconsistencies and uneven geographical distribution, and inversions of these data are usually controlled by assumed data weights and other model parameters. There are two major components in the numerical algorithm: the code that calculates initial ocean surface deformation due to coseismic displacements (Okada, 1985), and the nonlinear shallow water model of tsunami propagation and runup that employs the derived ocean surface deformation as an initial condition.

2.1 Tsunami data

Past studies of the coseismic slip distribution in the 1964 rupture provided a summary of the seismic, geologic and geodetic data sets, including their limitations and biases (Christensen & Beck, 1994; Holdahl & Sauber, 1994; Johnson et al., 1996; Santini et al., 2003; Ichinose et al., 2007; Suito & Freymueller, 2009). We focus here on the near-field observations and measurements of tsunami arrival time and runup, which have not been modeled before. Johnson et al. (1996) and Ichinose et al. (2007) used the far-field tsunami data and different subsets of the geodetic and seismic observations in joint inversion studies.

The near-field tsunami data consists of tsunami polarity and arrival times, tsunami wave amplitudes, runup heights and inundation zones (Wilson & Tørum, 1968; Plafker, 1969; Kachadoorian & Plafker, 1967; Plafker et al., 1969; Van Dorn, 1972). These data can only be used to constrain models where high-resolution grids of combined bathymetry and topography are available. The availability of such data sets is limited in Alaska, and there are just a few studies that have made use of them (Suleimani et al., 2003, 2010). Also, in order to study the tectonic tsunami source, we need to use only the data that were not altered by effects of local landslide-generated waves and seiches. This limits the data set to the outer coasts of the Kenai Peninsula and Kodiak Island. We selected those observations of the tectonic tsunami and compiled them in Table 1. The locations listed in the table are shown in Figure 1.

2.2 Numerical model and grids

We simulate tsunami propagation and inundation with a nonlinear shallow water model, which is formulated for depth-averaged water fluxes in both spherical and rectangular coordinates. The parallel numerical code solves the shallow water equations of motion and continuity using a staggered leapfrog finite-difference scheme. Nicolsky et al. (2010) provided a full description of the model, including its mathematical formulation and numerical implementation. This model was validated through a comprehensive set of analytical benchmarks and tested against laboratory and field data, according to NOAA's requirements for evaluation of tsunami numerical models (Synolakis et al., 2007, 2008). The algorithm is efficiently parallelized using the domain decomposition technique. The finite difference scheme is coded in FORTRAN using the Portable Extensible Toolkit for Scientific computation (PETSc). We use the equations of Okada (1985) for a finite rectangular fault to calculate the distribution of coseismic uplift and subsidence from the given slip model, the surface deformation is used as the initial condition for tsunami propagation.

We simulate the 1964 tectonic tsunami wave propagation on a set of nested telescoping bathymetric/topographic grids. These nested grids allow us to propagate waves from the deep waters of the tsunami source region in the Gulf of Alaska to shallow coastal areas of Kodiak Island and Kenai Peninsula (Figure 2). The external grid of the lowest resolution spans the entire North Pacific with a grid step of 2 arc-minutes, which corresponds to 1.85×3.7 km at latitude 60°N. The intermediate grids have resolutions of 24, 8 and 3 arc-seconds (387×740 m, 132×246 m, and 44×82 m, respectively). Bathymetry data for the low and intermediate resolution grids come from the ETOPO2 data set and

NOAA's National Ocean Service surveys. The computational time step is different for each grid and is calculated according to the Courant-Friedrichs-Levy (CFL) stability criterion. The numerical simulation used a constant Manning's roughness of 0.03 $s \cdot m^{-1/3}$.

3 Existing coseismic deformation models of the 1964 earthquake

The first complete rupture history of the 1964 earthquake was determined by Christensen and Beck (1994) from inversion of teleseismic P waves. They demonstrated that there were two areas of high moment release, representing the two major asperities of the 1964 rupture zone: the first and the largest moment pulse corresponded to the PWS asperity, and the second and smaller pulse of moment release was located in the KI asperity. A summary of the history of coseismic slip models is given in Supplemental Text S1. In this section we compare the static vertical displacement of the seafloor and tsunami predictions of the three most recent published models, and analyze results of numerical tsunami simulations in both the far and near field.

3.1 Review of previous studies

Johnson et al. (1996) performed a joint inversion of the tsunami waveforms and geodetic data, using a modified and simplified fault model based on Holdahl and Sauber (1994). The resulting model consists of 9 subfaults in the PWS asperity, 8 subfaults in the KI asperity, and one high-angle fault to represent the Patton Bay fault. Slip on the Patton Bay fault was limited to the rupture extent known at that time. Johnson et al. (1996) assumed a fault geometry that is consistent with the rupture on the Yakutat terrane - North American plate interface, with dip angles of 3° on the PWS subfaults, and dip angles in the KI region between 8° and 9°.

Ichinose et al. (2007) applied a combined inversion of seismic, tsunami and vertical (but not horizontal) ground displacements to estimate the spatial and temporal distribution of slip. The contribution of tsunami Green's functions was improved in this model compared to that in the joint inversion algorithm of Johnson et al. (1996) by introducing higher resolution grids surrounding the tide gauge stations and by using nonlinear hydrodynamic wave equations with a moving boundary condition. Their rupture model had three major areas of moment release, with the third asperity located beneath the continental shelf and slope, along the line that separates the PWS and KI segments in Figure 1. However, slip values in this model are much smaller than in the other models, and the total seismic moment is almost an order of magnitude lower.

The most recent model was introduced by Suito and Freymueller (2009). It was developed as a 3-D viscoelastic model in combination with an afterslip model, using realistic geometry with a shallow-dipping elastic slab. Important modifications in the fault geometry include a shallower dip angle (and thus also depth) for the megathrust in the Kodiak Island area. The authors used the model by Johnson et al. (1996) as a starting point for their coseismic slip model, adjusting it to the new geometry and critically reinterpreting the coseismic data, and then used forward modeling to optimize the model fit to vertical and horizontal geodetic displacements. The model also honors the horizontal coseismic displacements, which limits the extent of slip in the area of the western Kenai Peninsula. Notably, this study proposed that high slip on splay faults extended west along the entire length of the Kenai Peninsula, to explain how similar vertical displacements were observed over that length, even though the horizontal displacements were very different between the eastern and western Kenai Peninsula. The effects of splay fault displacements are negligible on the far-field tsunami amplitudes, but the first arriving waves in the near-field are very sensitive to this portion of the slip model.

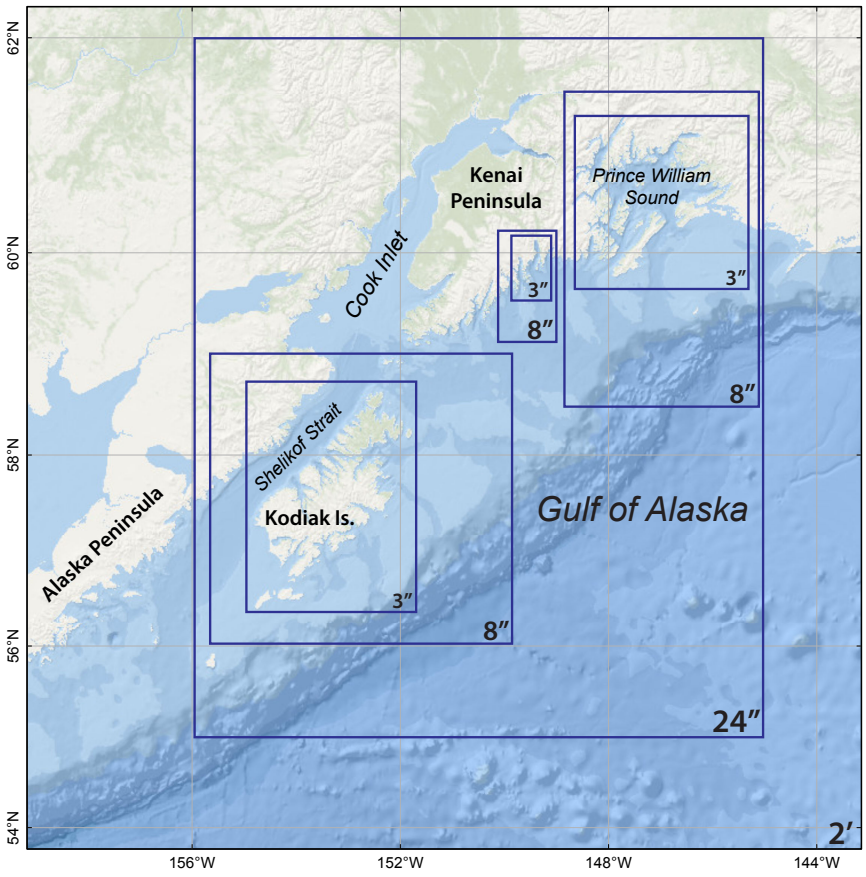

Figure 2. Embedded numerical grids of increasing resolution. The study area is covered by a grid with the resolution of 24 arc-seconds, which includes 3 grids of resolution of 8 arc-seconds around Kodiak Island, Prince William Sound, and Resurrection Bay. Each of the 8-arc-second grids includes a 3-arc-second grid.

3.2 Comparison of Tsunami Predictions for the Three Models

In this section we examine the tsunami predictions of the three most recent published coseismic slip models. We refer to these deformation models by abbreviations of the primary authors last names: JDM (Johnson et al. (1996)), IDM (Ichinose et al. (2007)), and SDM (Suito and Freymueller (2009)), respectively. We use a version of the SDM discretized for use with the Okada dislocation model (see Section 4.1 for details). None of these models considered the near-field tsunami arrivals, so this is an independent test of the predictive power of the models.

Figure 3 shows vertical coseismic deformation calculated for the three models. The deformation patterns differ in many key locations. The main difference in the IDM is that the slip and resulting deformation in the Prince William Sound region is much smaller and more restricted than in the other models. The SDM has larger vertical motions in general because of the shallower fault dip and depth compared to the other models. The area of larger uplift offshore Kodiak Island is located more to the northeast in JDM compared to the others. Only the SDM has the entire coast of Kodiak Island in a subsidence regime. Unlike the JDM or IDM, the SDM has distinct paired uplift/subsidence band running the entire length of the Kenai Peninsula, due to slip on the splay fault.

Figure 3 also presents the distribution of tsunami energy calculated from the tsunami propagation model for the three source functions, for the near-field and far-field. These plots show the maximum computed tsunami amplitudes during the first 12 hours of wave propagation simulation. Over the entire model run, only the maximum tsunami amplitude was stored for each grid point. All three tsunami sources show strong directivity of energy radiation toward the west coast of the US and Canada, which confirms the findings of Ben-Menahem and Rosenman (1972) that the 1964 tsunami had a pronounced beaming effect. Although the three far-field patterns are visually distinct in the open ocean, the model predictions at the distant tide gauge locations are all very similar (see Supplementary figures).

However, the near field shows dramatic differences between the three source functions. Even though the SDM is quite similar overall to the JDM, the change in the megathrust dip and change in the splay fault extent have a substantial impact on the near-field tsunami predictions, both in terms of the maximum energy distribution and the time series of predicted wave heights. The IDM and JDM source models do not generate a good match to tsunami arrivals along the Kenai Peninsula and Kodiak Island coasts. Both the IDM and JDM failed to match the wave arrivals and amplitudes at Seward and Naval Station, the critical locations where tsunami arrivals were best documented, while SDM predicted these arrivals very well (Figure 4). A more detailed comparison of all three models is given in Suleimani (2011). The large discrepancies show that the JDM and IDM source functions do not adequately describe the near-field tsunami waves, so our further studies of the slip distribution are based primarily on the SDM.

4 An optimized source function of the 1964 tsunami

The spatial extent of the splay fault ruptures is a key question both for tsunamigenesis and for understanding the persistence of the PWS asperity (Liberty et al., 2019). Therefore, we reassess and optimize the tsunami source function, starting with the SDM model of Suito and Freymueller (2009), and use the near-field observations from the Kenai Peninsula to assess the lateral extent of splay faulting. We analyze the near-field tsunami arrival times and polarity of first arrivals to constrain the submarine extent of the splay fault.

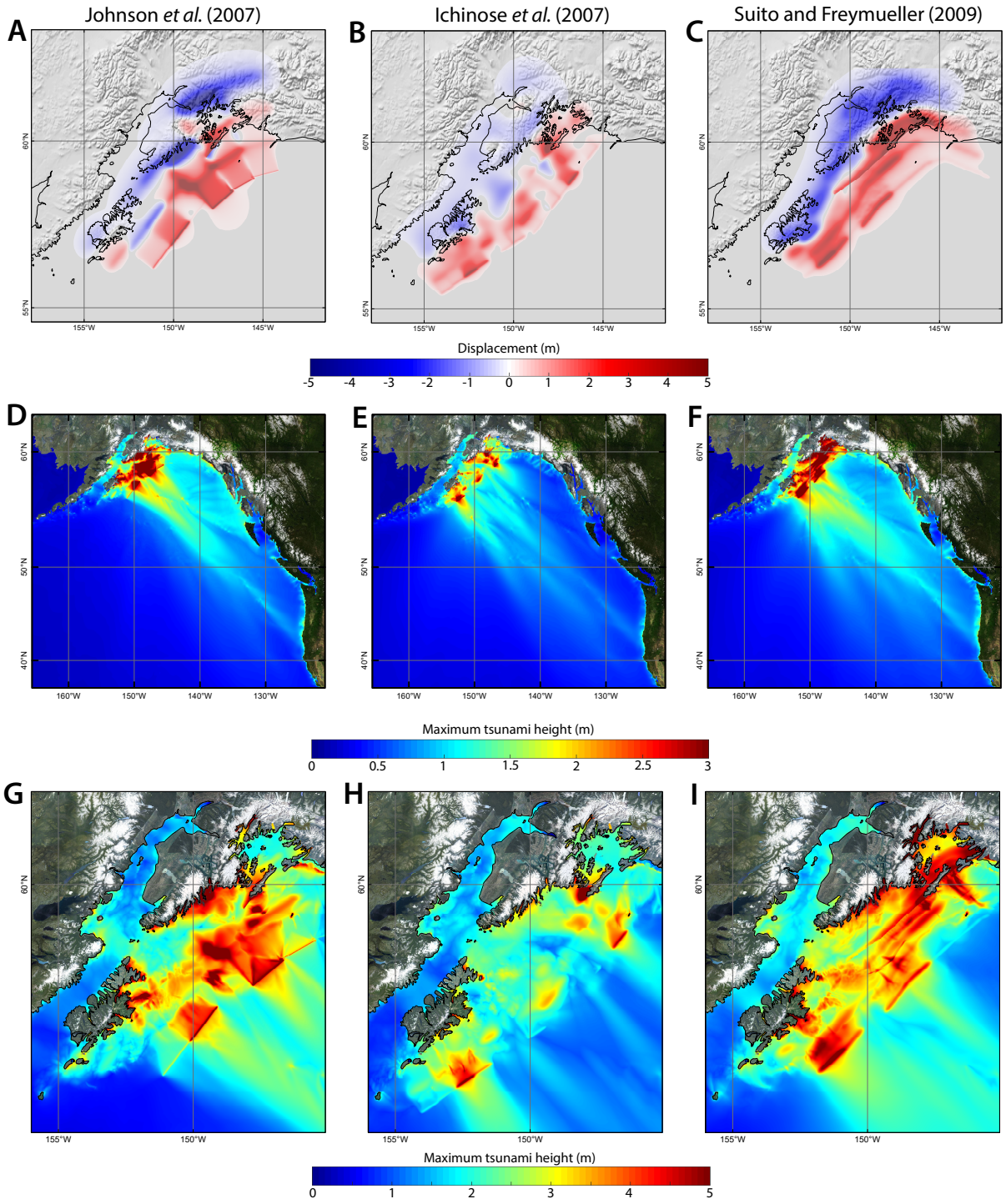

Figure 3. Vertical coseismic displacements, and maximum tsunami amplitudes based on the slip models of Johnson et al. (1996) (left column), Ichinose et al. (2007) (center column), and Suito and Freymueller (2009) (right column). The top row shows the predicted vertical deformation, middle row shows the near-field maximum tsunami heights, and the bottom row shows the far-field maximum tsunami heights.

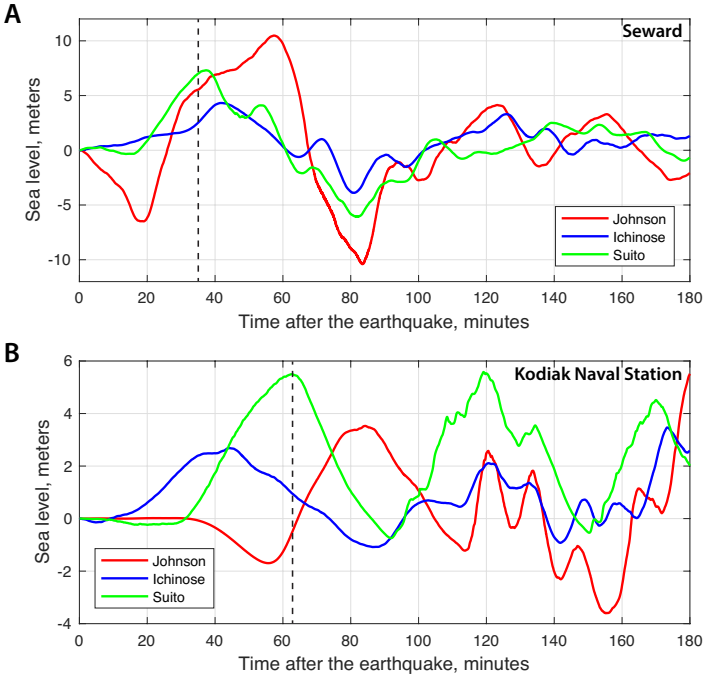

Figure 4. Time series at Seward (A) and Kodiak Naval Station (B) calculated using the source functions by Johnson et al. (1996), Ichinose et al. (2007), and Suito and Freymueller (2009). The black dashed line on each plot indicates the observed arrival time at this location (see Table 1). The polarity of the first arrival at both locations is positive.

4.1 Discretization of the fault geometry

The fault geometry and slip distribution of Suito and Freymueller (2009) (large colored patches in Figure 5a) were defined within a finite element model mesh. The slip model consists of 36 elements, with a single value of slip assigned to each element. However, these polygons are not rectangles and the mesh surfaces within each element are not planar as required for the standard Okada (1985) dislocation source, so we re-discretized the SDM slip model onto a set of planar sub-faults compatible with the Okada (1985) dislocation equations. The finite element model of Suito and Freymueller (2009) used elements that are parallelograms of different sizes, so we first discretized each SDM polygon into a number of small parallelograms. Then, we approximated each of the parallelograms with the best-fit rectangle of the same area and strike, preserving the seismic moment. As a last step, we recalculated the values of dip and rake angles based on Okada's conventions, accounting for any small changes in the sub-fault orientation. We also corrected the position of the splay fault line with respect to the Montague Island coast, since in the original model it was shifted to the south by a distance approximately equal to the width of the south-western part of the island. This was probably a digitization error by Suito and Freymueller (2009). We moved the appropriate splay fault elements so that the model fault coincides with the mapped section of the fault on Montague Island, digitized from a geologic map by Tysdal and Case (1979). The resulting Okada-type discretization of the fault geometry is presented in Figure 5. This rupture model has total seismic moment of 7.7×10^{22} Nm with a rigidity of 50 GPa, as given in Suito and Freymueller (2009). The resulting coseismic deformation of the 1964 rupture calculated using Okada (1985) for each subfault, is shown in Figure 3c.

4.2 Splay fault contribution to the local tsunami wave field

To determine the extent of the active splay faulting in 1964, we analyze tsunami arrival times and polarity of the first arrivals to four locations on Kenai Peninsula, for which observations are available: Rocky Bay, Seward, Whidbey Bay and Puget Bay (Figures 1 and 5b; Table 1). We divide the southwestern extension of the fault into 11 segments that correspond to the elements in the fault model (Figure 5b). We could construct as many as 11 source functions by removing segments one by one from the southwestern extension of the fault. However, having data from only 4 locations, we can distinguish only a few major cases for comparison and analysis - the case with the full model length; the case with 4 segments removed from its southwestern end; the case with 7 segments removed; and the case where the length corresponds only to its sub-aerial mapped extent (Figure 5b).

We modeled the displacements and tsunami propagation using these 4 cases as the initial conditions in the tsunami model. The different lengths of the splay fault affect the deformation pattern only in the vicinity of the Kenai Peninsula, changing the amount of subsidence along the shore and the position of the hinge line that separates areas of tectonic uplift and subsidence (Suleimani, 2011). The calculated time series at the four locations are shown in Figure 6. The position of zero water level on each plot was adjusted to reflect the post-earthquake sea level, since Rocky Bay and Seward subsided during the earthquake, while Whidbey Bay and Puget Bay experienced tectonic uplift.

We also investigated the impact of changes in the splay fault model on the far-field tsunami waveforms. Johnson et al. (1996) assumed that contribution of the Patton Bay fault to the far-field tsunami waveforms was small enough to be neglected. We found that the inclusion of the splay fault into the source function does not change either the arrival times or the wave amplitudes of the first arrival for any of the far field locations (see Supplementary figures and Suleimani (2011) for more details), which confirms the assumption of Johnson et al. (1996). At some far-field locations the splay fault has a minor effect on the later arrivals.

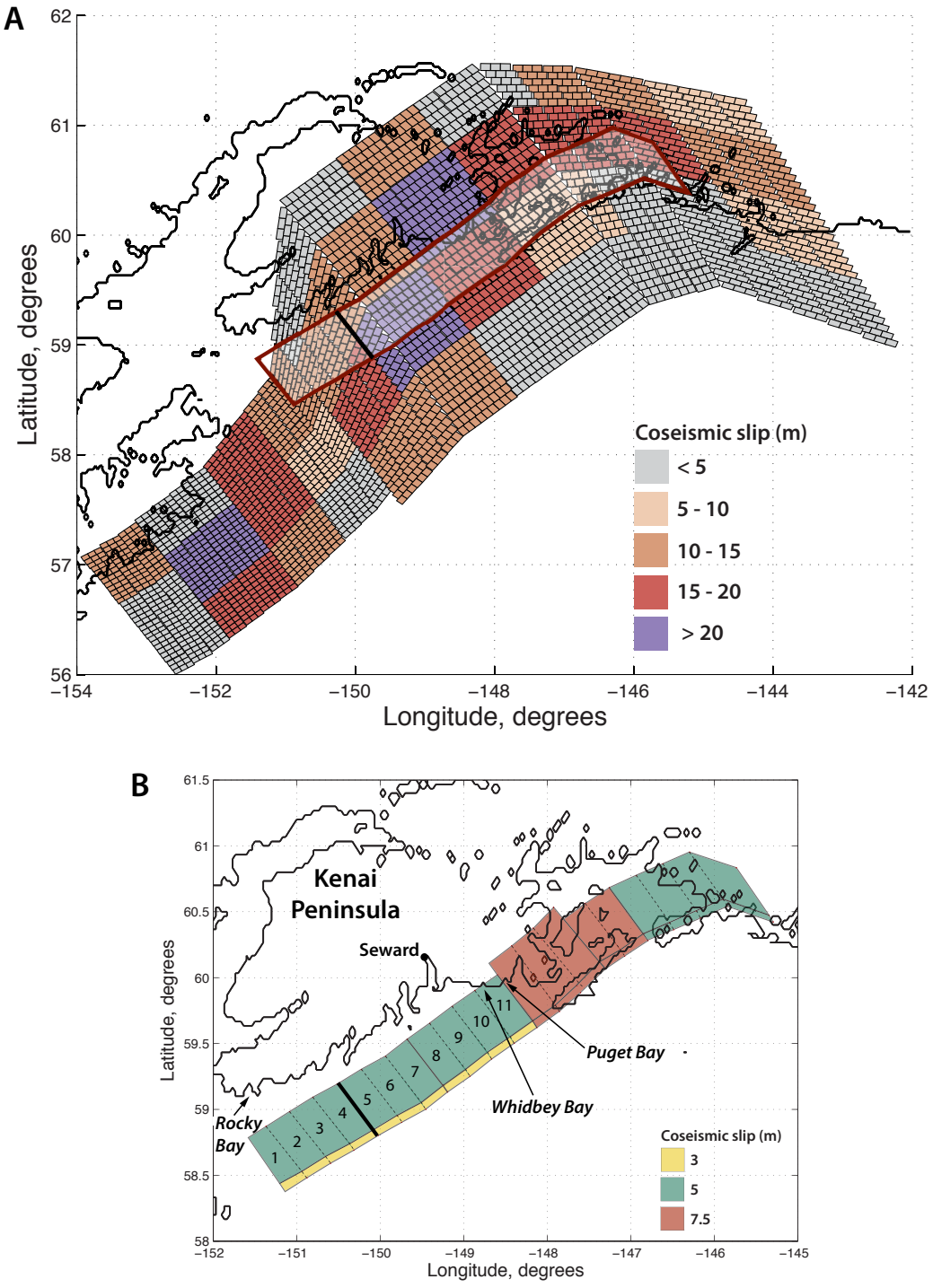

Figure 5. (A) Discretization of finite elements of the slip model by Suito and Freymueller (2009) using the rectangular Okada-type subfault elements. Combined discretized models are shown for the geometry of megathrust and the splay fault. (B) The splay fault is divided into 11 segments to test for its spatial extent. The thick line shows the western edge of slip inferred on the splay fault after our tests.

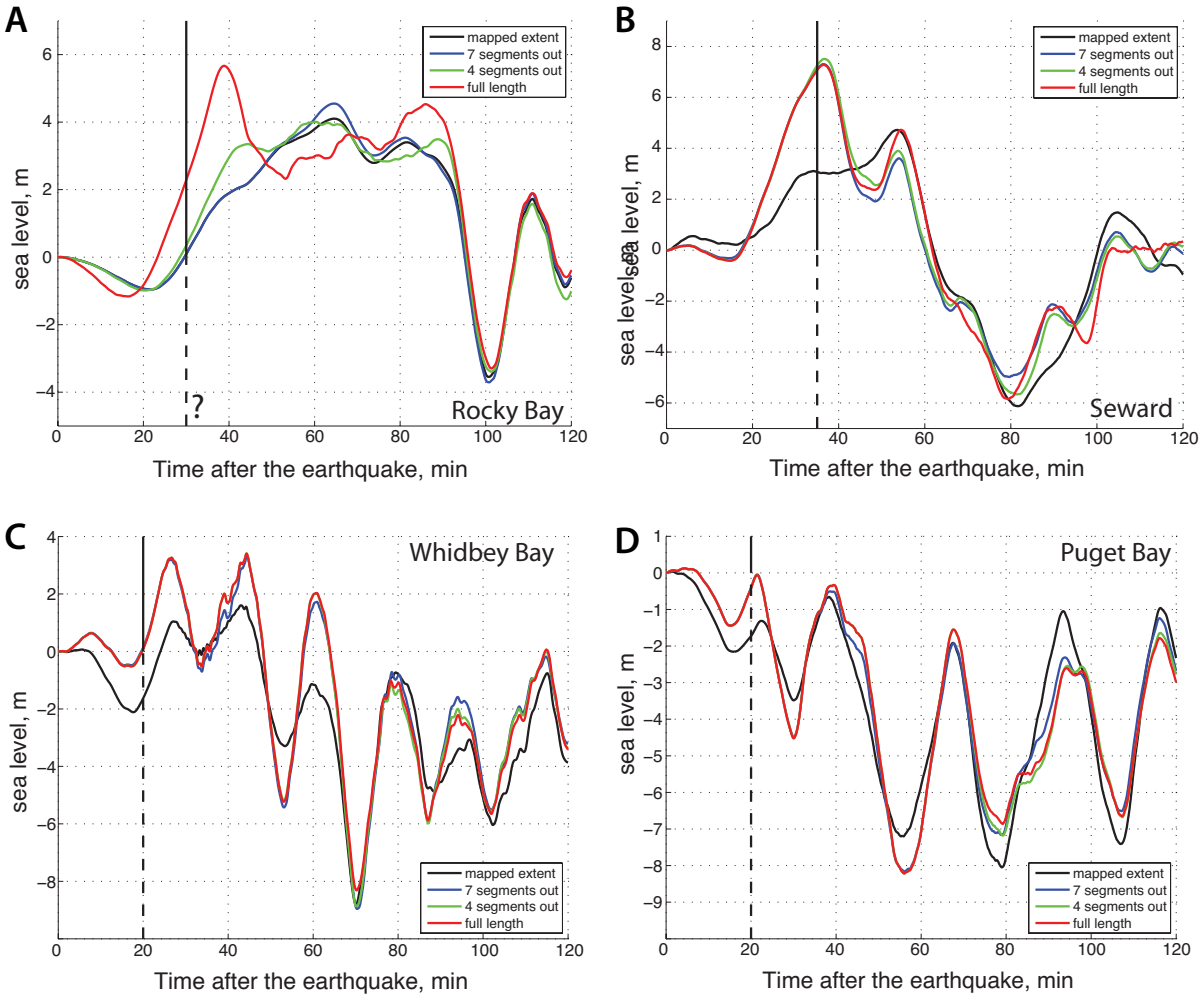

Figure 6. Simulated time series of tsunami waves at (A) Rocky Bay, (B) Seward, (C) Whidbey Bay, and (D) Puget Bay for 4 different lengths of the splay fault. The black line on each plot indicates the observed arrival time at this location (see Table 1). The question mark in plot A indicates that the observation of arrival time of the tsunami crest is uncertain.

Rocky Bay. Rocky Bay is a critical location for our study, because it is at the end of the proposed extension of the splay fault. It was the site of a small logging camp, which subsided about 1.5 meters during the earthquake. The first crest was about 2.7 meters high and arrived about 30 min after the earthquake, but the eyewitness did not pay much attention to the time of wave arrivals (Plafker et al., 1969). It was noted, however, that the first crest was preceded by a withdrawal. The calculated time series at Rocky Bay are shown in Figure 6a. It is obvious that the full-length splay fault generates an amplitude that is too high, and the crests that correspond to sources with the sub-aerial mapped extent of the fault and with the 7 segments removed, arrive too late. The source with 4 segments removed fits observations better than others sources do. Also, the calculated arrival time of about 40 minutes after the earthquake seems logical, since at about 30 minutes the waves were reported at Seward with a high degree of accuracy. If the splay fault did not extend as far as the end of the Kenai Peninsula, then it would take the waves additional time to reach Rocky Bay.

Seward. The town of Seward in Resurrection Bay is the only location along the Kenai Peninsula coast that has a detailed and reliable record of tsunami waves (Lemke, 1967). Seward suffered from the combined effects of local landslide-generated waves and the major tectonic tsunami. The locally generated wave at Seward was about 6-8 m high, and struck about 1.5-2 minutes after the shaking began. The tectonic tsunami wave came into the bay about 30 to 35 minutes after the beginning of the earthquake, and it was as high as the landslide-generated wave (Plafker, 1969; Wilson & Tørum, 1968; Lemke, 1967). The Seward time series in Figure 6b demonstrates that all sources except for the fault with the mapped extent provide a very good match to both the arrival time and the observed amplitude. The simulated waves arrive just 2 to 3 minutes later than the observed wave, which could be due to the splay fault being too far from the shoreline in our model. The Seward results clearly demonstrate that the tectonic wave, which came to Resurrection Bay about 30 minutes after the earthquake, was generated by displacements on the splay fault, and that the splay fault definitely extended beyond its sub-aerial mapped length.

Whidbey Bay. An eyewitness at the small logging camp located at the head of Whidbey Bay recorded the arrival of the first wave at 19.5 minutes after he felt the first shock (Plafker et al., 1969). This wave ran up to an estimated elevation of 10 meters above mean lower low water. It is hard to estimate the runup height from the tsunami wave amplitude without detailed inundation modeling, but we can estimate the wave amplitude in the bay offshore. The time series in Figure 6c shows that the simulated wave arrives about 6 minutes too late. Since the documented arrival is a reliable observation, it means that the source of the wave crest in the model is too far away from the shore in the vicinity of Whidbey Bay; this might be explained if the splay fault were slightly closer to the coast than we have modeled. The time series show that the only scenario that greatly underestimates the amplitude of the wave is the one restricted to the mapped extent of the fault. Also, that scenario generates a significant initial water withdrawal, which is contrary to the observations. Whidbey Bay data thus also require the splay fault slip to extend beyond the sub-aerial mapped extent of the fault on Montague Island.

Puget Bay. A small logging camp in Puget Bay was badly damaged by tsunami waves (Plafker et al., 1969). The area experienced tectonic uplift of about 1.5 m. The first wave arrived 20 minutes after the earthquake (Plafker et al., 1969), which agrees with the calculated time series in Figure 6d. Again, the plot shows that the only scenario that stands alone is the scenario that uses only the sub-aerial mapped extent of the fault. The amplitude of the first wave seems too low in order to make an observed runup of 5.5 m. This discrepancy could result from overestimation in the model of coseismic uplift at Puget Bay - the calculated uplift there is between 3 and 4 meters versus 1.5 meters of observed uplift.

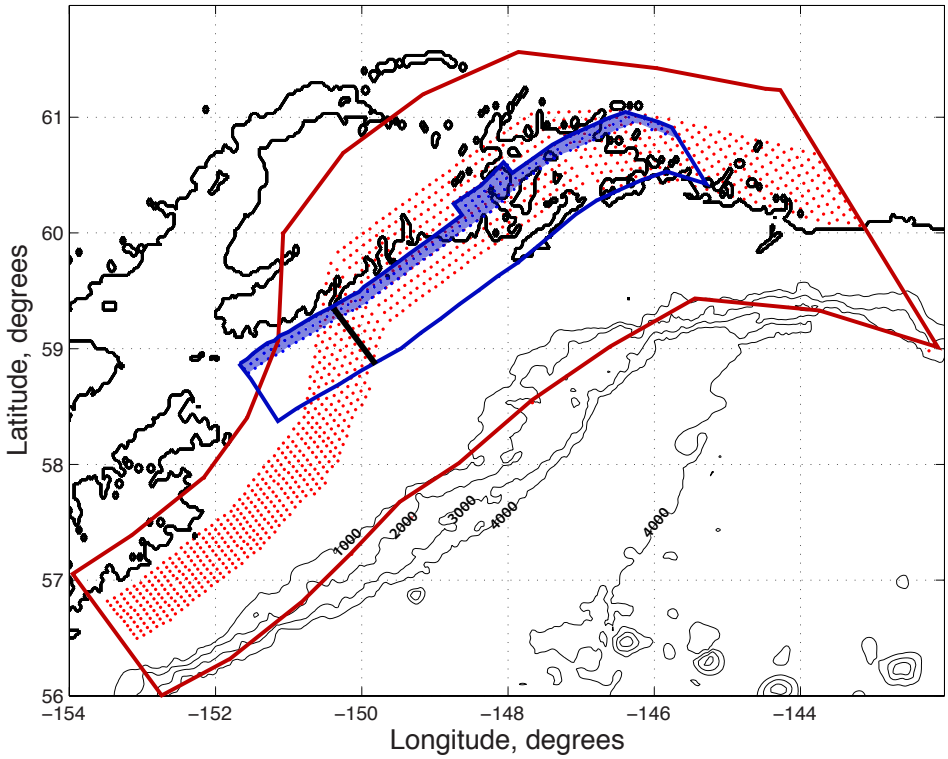

Figure 7. The location of the splay fault (blue polygon) with respect to the rupture on the megathrust (red polygon) in the coseismic model. The red dots indicate locations of the megathrust subfault elements that are between 18 and 25 km deep in the model. The blue shaded area inside the splay fault polygon are the elements located within the same depth band. The thick line indicates the inferred western limit of slip on the splay fault. The bathymetry contours show the steepest part of the ocean slope between 1000 and 4000 meters deep.

The analysis of the tsunami time series along the southern coast of the Kenai Peninsula, and results of tsunami inundation modeling at Seward (Suleimani et al., 2010), allow us to conclude that the splay fault extends as far as the boundary between the 4th and 5th segments in Figure 5, but not as far as the western tip of the peninsula. To find possible explanations for this result, we investigated the connection of the splay fault and the megathrust by plotting subfault elements of both models within the depth band of 18 to 25 km, within which the deepest part of the splay fault is located (Figure 7). Figure 7 shows that at about 150°W the splay fault disconnects from the megathrust, due to the increasing dip angle of the megathrust to the west.

If we assume that the splay fault is not an independent source that ruptured separately from the megathrust in the previous events, but rather a feature that gets triggered only by megathrust earthquakes, then it has to be connected to the megathrust. In addition, in that case slip on the splay fault could occur only where there was also significant slip on the megathrust. Therefore, we would expect slip on the splay fault to terminate at the same longitude as the SW end of the Prince William Sound asperity. We find that the end of the splay fault at 150°W corresponds both to the edge of the asperity in the SDM, and to the lateral boundary of interseismic slip deficit (Suito & Freymueller, 2009; Zweck et al., 2002; Li et al., 2016).

4.3 Contribution of horizontal displacements to tsunami generation

In many tsunami studies in the past, the effect of horizontal displacements was neglected when the ocean surface deformation was calculated as an initial condition for tsunami propagation. However, it has been shown by a number of authors that a tsunami can be generated by horizontal motions of the sea floor if horizontal displacements generate a significant portion of the ocean surface uplift by moving a sloping surface (Tanioka & Satake, 1996; Jamelot et al., 2019; Heidarzadeh et al., 2019; Ulrich et al., 2019). This generation mechanism is illustrated by the diagram in Figure 8. Song et al. (2008) analyzed seismically-inverted sea floor deformation of the 2004 Sumatra-Andaman earthquake and found that the vertical displacements alone were not sufficient to generate the powerful tsunami, and that two thirds of the satellite-recorded tsunami wave height was due to the horizontal displacements. In that case, the horizontal motions generated kinetic energy 5 times larger than the potential energy due to the vertical motion, and the directivity pattern of tsunami energy propagation was also best explained by including horizontal forcing into the source mechanism.

The faulting geometry of the 1964 earthquake suggests that its coseismic horizontal displacements could have had a sizable contribution to the tsunami amplitudes. First, the earthquake mechanism was a shallow-dipping thrust, with dip values changing from 4.5° in the PWS asperity to 7.9° in the Kodiak asperity (Suito & Freymueller, 2009). Second, a significant amount of coseismic deformation occurred in the area of the steep slopes of the Aleutian trench in the Gulf of Alaska. The horizontal displacement over Prince William Sound and the Kenai Peninsula was directed mostly to the southeast, that is nearly perpendicular to the trench. Plafker (1969) found that the areas of maximum horizontal displacements generally coincided with maxima of vertical displacements, and that the horizontal displacement vectors were approximately normal to the isobases.

We set up a numerical modeling experiment to study the contribution of horizontal displacements to the tsunami wave field. One limitation of our model is in its ability to account only for the static vertical deformation of the ocean surface that results from horizontal motion of the bottom. The other component, which is transfer of kinetic energy from a moving slope into the water column, cannot be simulated in the current model. We construct two tsunami sources - one that includes the vertical deformation due to horizontal displacements, and one that was derived using the vertical displacements only. Then, we compare tsunami wave heights and arrival times generated by the two sources in the near and far field.

According to Tanioka and Satake (1996), the vertical displacement of the ocean surface, ξ_h, resulting from the horizontal motion of the ocean bottom slope can be calculated as the dot product of the horizontal displacement vector $\vec{d}$ and the gradient of the bottom slope:

$$\xi_h = d_x \frac{\partial H}{\partial x} + d_y \frac{\partial H}{\partial y}, \tag{1}$$

where H is bathymetry, and d_x and d_y are the east-west and north-south components of the horizontal displacement vector. We calculated the bottom slope gradients over the 1964 deformation area in the 24-arcsecond grid that covers Gulf of Alaska (Figure 2), and used the equations of Okada (1985) to derive the horizontal displacement vectors on the same grid. The resulting vertical deformation is presented in Figure 9a. The plot shows a number of important features of the deformation field. First, the areas of maximum deformation due to horizontal displacements coincide with the regions where vertical displacements were also large. Second, the maximum deformations are distributed within the band of large bathymetry gradients. There are two pronounced maxima in the displacement field - one in the Kodiak asperity south-east of Kodiak Island, and the second one in the PWS asperity, south of Montague Island. The maximum value of the vertical deformation due to horizontal displacements is 1.55 m. Another interesting feature of the displacement field is the initial depression of the sea surface by about 0.5 m

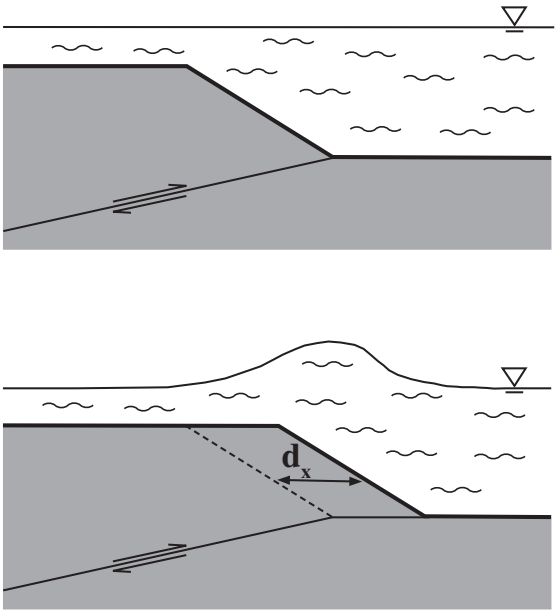

Figure 8. The diagram shows mechanism of tsunami generation by horizontal motion of the ocean bottom, where d_x is the horizontal displacement due to faulting (modified from Tanioka and Satake (1996)).

in the eastern parts of Cook Inlet and Shelikof Strait. Waller (1966) reported waves observed in Cook Inlet and Kachemak Bay within 5 minutes after the main shock, traveling perpendicular to the shores. These waves have remained unexplained until now, because no evidence of slumping or sliding was found. We propose that the waves could be seiches generated by the tilting of the sea surface due to horizontal motion of the water basin.

We calculated the maximum tsunami amplitudes for only the effects of the horizontal displacements as shown in Figure 9a (the direct vertical displacements are not included). Since vertical and horizontal deformation occur together during the rupture process, the tsunami source in this experiment is hypothetical, but it helps to estimate where the effects of the added deformation due to horizontal displacements could be significant in the near field. Figure 9b shows maximum tsunami amplitudes in the Gulf of Alaska generated only by horizontal displacements. It demonstrates that the tsunami energy from the deformation maximum in the Kodiak asperity is directed toward the section of the Kodiak coast between Cape Chiniak and Dangerous Cape (see Figure 1 for locations). This stretch of the coast is the area of the maximum measured runup on Kodiak (Plafker and Kachadoorian (1966); see also Section 4.4). The second deformation maximum in the PWS asperity generates tsunami waves whose energy is directed toward the coast of Kenai Peninsula, west of Resurrection Bay. There are no measurements or observations of tsunami in that area.

The contribution of the horizontal displacements varies considerably from place to place. For far field sites along the Pacific coast of the United States and Canada, the amplitudes are 10 to 18% larger for the source that includes horizontal displacements (see Supplemental Figures). The effect is mostly evident in the first arrival, while the splay fault affects the waveforms later during the tsunami propagation span. On the coast of Kodiak island, the waveforms are almost identical in shape, and the amplitude was 5 to 7% larger for the source that included vertical deformation due to horizontal bottom motion (Figure 10).

A study of horizontal impulses of the continental slope during the 2004 Sumatra-Andaman earthquake concluded that the momentum force they generated was the major contributor to the tsunami wave height and to the tsunami directivity pattern (Song et al., 2008). Similarly, in the case of the 1964 earthquake the horizontal motion of the bottom slope was directed seaward, mostly to the southeast. This means that the kinetic energy transferred to the water from the moving bottom was directed toward the west coast of the United States and Canada. The potential energy of the 1964 tsunami computed for the coseismic model that includes effects of the splay fault and horizontal displacements is 4.1×10^{15} J. The potential energy estimated by Lay et al. (2005) for the 2004 Sumatra-Andaman earthquake was 4.2×10^{15} J, almost the same. In order to estimate the relative importance of the kinetic energy transfer during the 1964 earthquake, we used an algorithm similar to that described in Song et al. (2008) to estimate the displacement velocity of the seafloor as a function of time. In the absence of time-dependent seafloor displacements, we estimated the velocities by analogy to the 2003 Tokachi-Oki earthquake, for which 1-Hz GPS records gave an average time of 20 seconds for the displacement to occur at any one place (Emore et al., 2007). The kinetic energy of the 1964 tsunami corresponding to displacement times of 10, 20 and 30 seconds is 7.6×10^{15} J, 1.9×10^{15} J, and 8.4×10^{14} J, respectively. This range of values demonstrates that this simple model for estimation of kinetic energy is very sensitive to the duration of the seafloor motion, and even the slow case produces the kinetic energy that is at least 20% of the potential energy. We can therefore assume that underestimation of the 1964 tsunami wave heights at tide gauges located along the US west coast by many existing models could result from not accounting for the momentum force in tsunami genesis. To test this hypothesis, we would need to develop a fully coupled earthquake-tsunami generation model

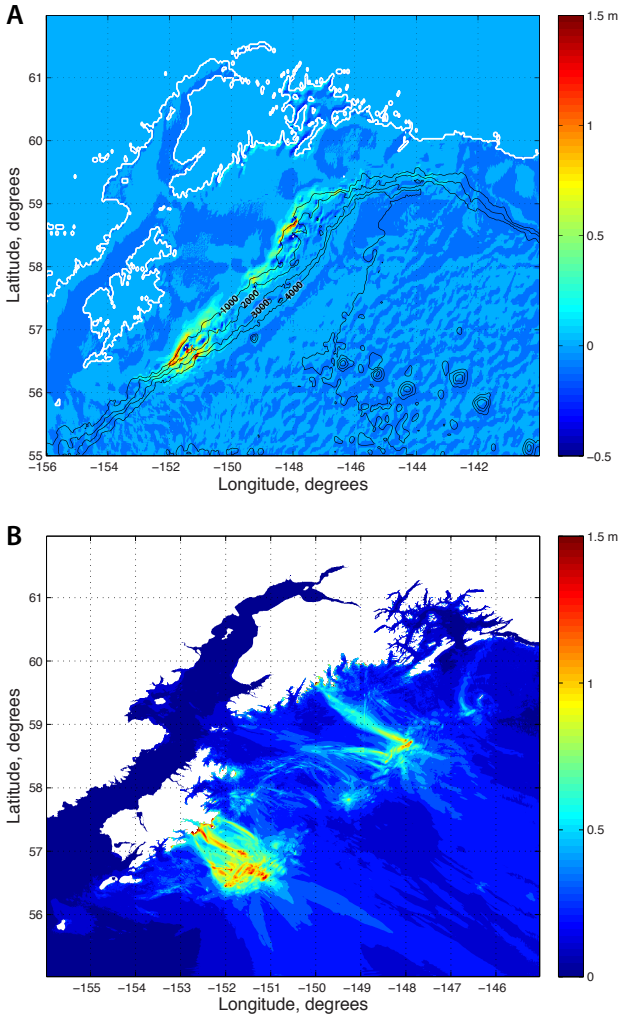

Figure 9. (A) Calculated sea surface displacement due to horizontal motion of the sea floor during the 1964 earthquake. The white contour corresponds to the coastline, and the black lines are bathymetry contours that indicate the steepest part of the trench that is between 1000 and 4000 meters deep. (B) Maximum tsunami heights due to horizontal displacements of the sloping ocean bottom.

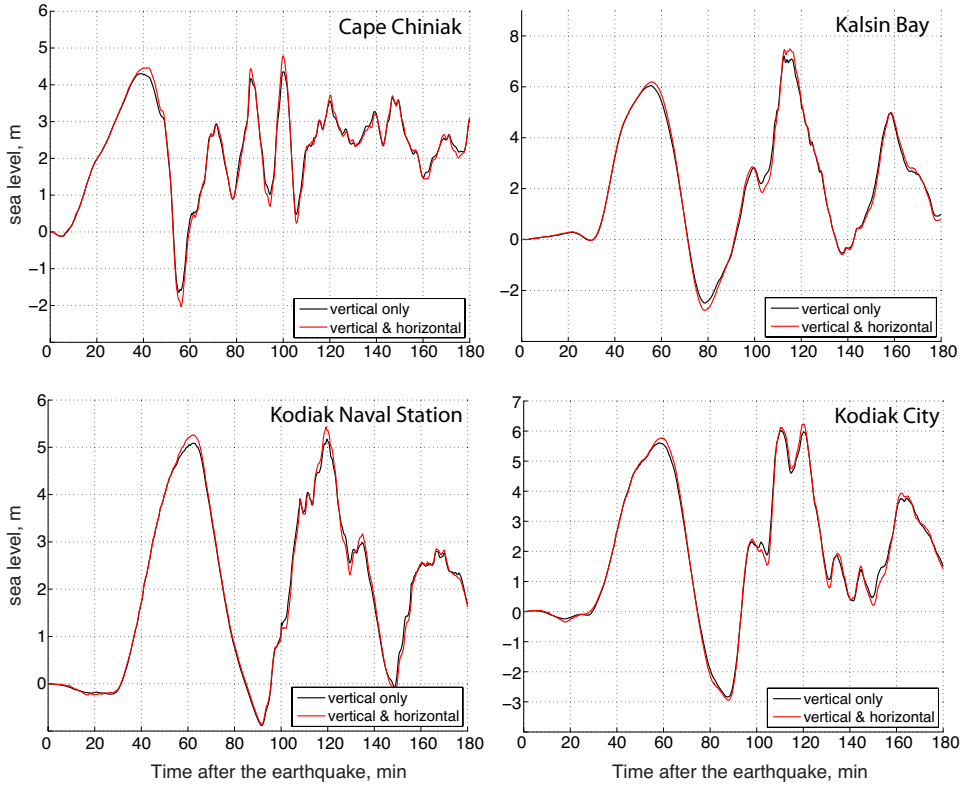

Figure 10. Simulated time series of tsunami waves generated by vertical motion of the bottom (black line) and by the combined vertical and horizontal motion (red line).

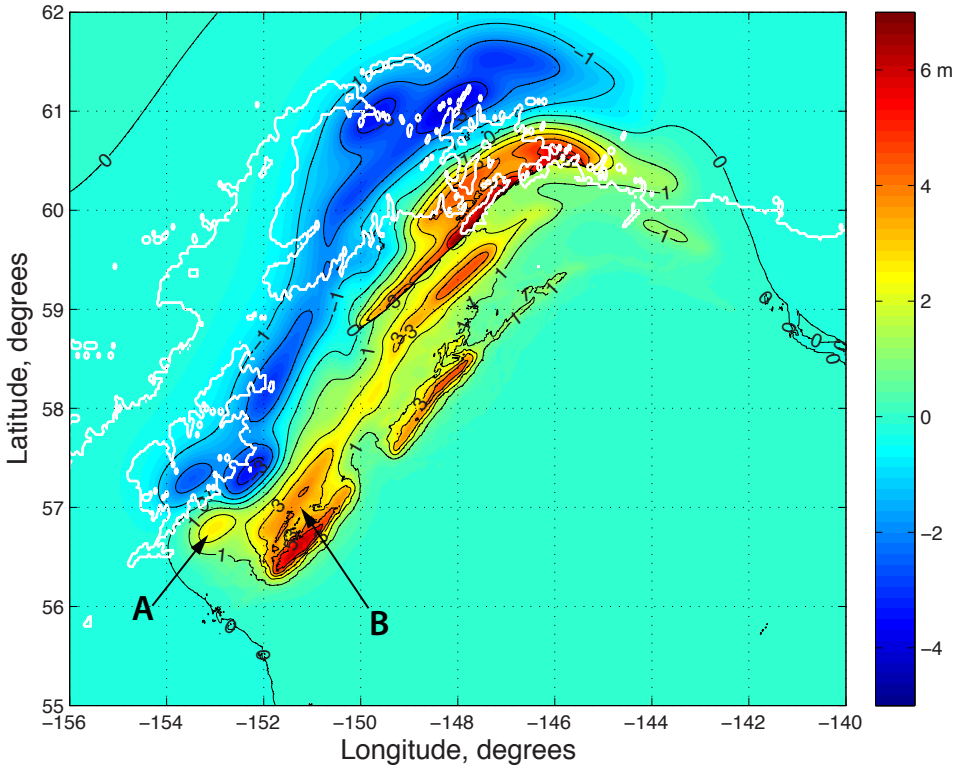

Figure 11. The resulting vertical coseismic deformations in the 1964 rupture area, derived from the superposition of vertical and horizontal displacements of the megathrust and the vertical displacements on the splay fault of the optimal extent.

that allows for the time-dependent kinetic energy transfer from the bottom motion into the water column.

To summarize our findings discussed in Sections 4.2 and 4.3, we provided new constraints on the extent of the splay fault along the southern shore of the Kenai Peninsula, and investigated the horizontal displacements contribution to tsunami amplitudes. Figure 11 shows the superposition of three deformation fields: the uplift of the ocean surface due to vertical displacements on megathrust, that due to coseismic horizontal motion of the ocean bottom, and uplift due to displacements on the splay fault, which extends to about 150°W.

4.4 Coseismic slip in the Kodiak asperity

Suleimani et al. (2003) showed that the results of the near-field inundation modeling strongly depend on the slip distribution within the rupture area, because the complexity of the source function is in close proximity to the coastal zone. While the calculated runup in that study, based on the model of Johnson et al. (1996), agreed relatively well with the observed inundation, the calculated and observed arrival times at the Kodiak Naval Station were out of phase. Since the arrival times are more sensitive to the fine structure of the tsunami source than the inundation area, we test the arrival times predicted by our updated source function, including the modifications to the splay fault, to see if it can better predict the near-field arrival times. The deformation of the ocean bottom in this area generated destructive tsunami waves that reached the exposed eastern shore of Kodiak Island between 20 minutes and 1 hour after the earthquake. The

tsunami waves had catastrophic effects on Kodiak Island communities during and after the earthquake, causing 18 deaths and extensive property damage (Plafker & Kachadoorian, 1966).

We apply the updated source function (Sections 4.2 and 4.3), and generate the initial ocean surface displacements using formulas by Okada (1985), including the effect of the horizontal displacements. We simulate propagation of tsunami waves as described in Section 3.2. The maximum-amplitude plot presented in Figure 12a shows a number of interesting results. First, it supports the observation that the waves were high and destructive only along the eastern exposed ocean coast of Kodiak Island, and that waves along the southwest coast and on the Shelikof Strait side of the island were small and did not inundate above the normal high tide levels (Plafker & Kachadoorian, 1966). Second, the numerical results show a concentration of the highest waves at the coastal locations exactly where the highest runup was measured: at the uninhabited shore between Cape Chiniak and Narrow Cape, and on the southeast beach at Sitkalidak Island. These locations are marked by black crosses in Figure 12a. The horizontal deformation component contributed to the higher tsunami amplitudes along the shoreline between Cape Chiniak and Dangerous Cape (see also Figure 9b, which shows maximum tsunami amplitudes generated by horizontal displacements only).

These results demonstrate that that the calculated directions of tsunami energy concentration in the vicinity of Kodiak Island agree well with the observations of tsunami impact in 1964. At some locations the maximum runup was caused by the first wave, which was the largest one even though it arrived on low tide, but in many places the highest runup coincided with high tide, which came about 6 hours after the earthquake (Plafker & Kachadoorian, 1966; Plafker et al., 1969; Wilson & Tørum, 1968). Therefore, we need to examine arrival times as reliable indicators of the spatial origins of the leading tsunami wave crest. To do that, we analyze time series at several locations on Kodiak Island along its south-eastern shore, which was exposed to the initial impact of tsunami waves (Figure 12a).

Kaguyak. Wilson and Tørum (1968) reported that the first wave arrived at the small fishing village of Kaguyak about 20 minutes after the earthquake, which agrees well with the modeling results (Figure 13a). This first wave originated in the area of higher slip just offshore the southern tip of the island, marked by the letter "A" in Figure 11. The initial ocean surface displacements generated by the updip vertical motions due to slip on the megathrust are marked by the letter "B". Estimating the speed of the wave front as $c = \sqrt{gH}$, where g is the acceleration of gravity and H is the water depth, we calculate that it took the waves originating in area B about 55 minutes to reach the coast, which agrees well with the arrival time of the second crest at Kaguyak. The arrivals of both crests are clearly visible in Movie S1.

Old Harbor. This village is located in the Sitkalidak Strait that separates Kodiak and Sitkalidak Island. It was almost entirely destroyed by tsunami waves. The initial wave struck the community 48 minutes after the earthquake ((Kachadoorian & Plafker, 1969)). The modeled arrival is in good agreement with observations (Figure 13b).

Cape Chiniak. 38 minutes after the start of the earthquake, the Fleet Weather Central at the Kodiak Naval Station received a report from the US Coast Guard station about the arrival of a big tsunami wave at Cape Chiniak (Plafker & Kachadoorian, 1966). This warning resulted in evacuation of residents in the Kodiak area, which saved many lives. The calculated arrival time agrees well with the observations. The wave height was estimated by eyewitnesses to be about 30 feet (9 meters). The simulated amplitude is about half of that value (Figure 13c). The first wave at Chiniak originated at the area of high slip marked by letter "B" in Figure 11. In addition to consistent overestimation of tsunami amplitudes by eyewitnesses, the discrepancy could indicate too low values of slip in this section of the Kodiak asperity.

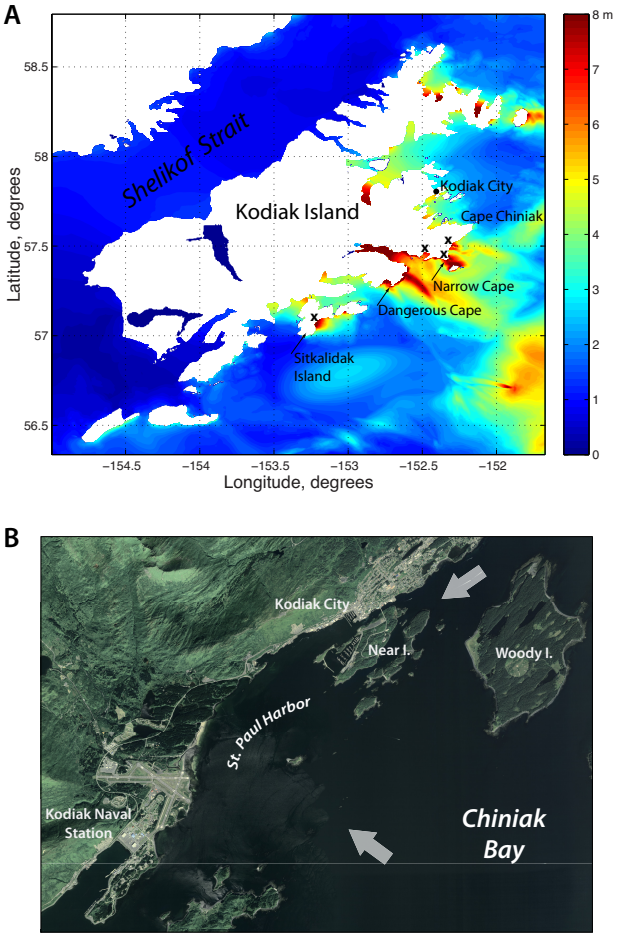

Figure 12. (A) Simulated maximum tsunami amplitudes in the 8-arcsecond grid of Kodiak Island. The initial conditions correspond to the deformation model shown in Figure 11. Black crosses indicate localities of the highest measured runup (Plafker & Kachadoorian, 1966). (B) Kodiak City and Kodiak Naval Station in the St. Paul Harbor. Arrows indicate major directions, from which the 1964 tsunami waves entered the harbor.

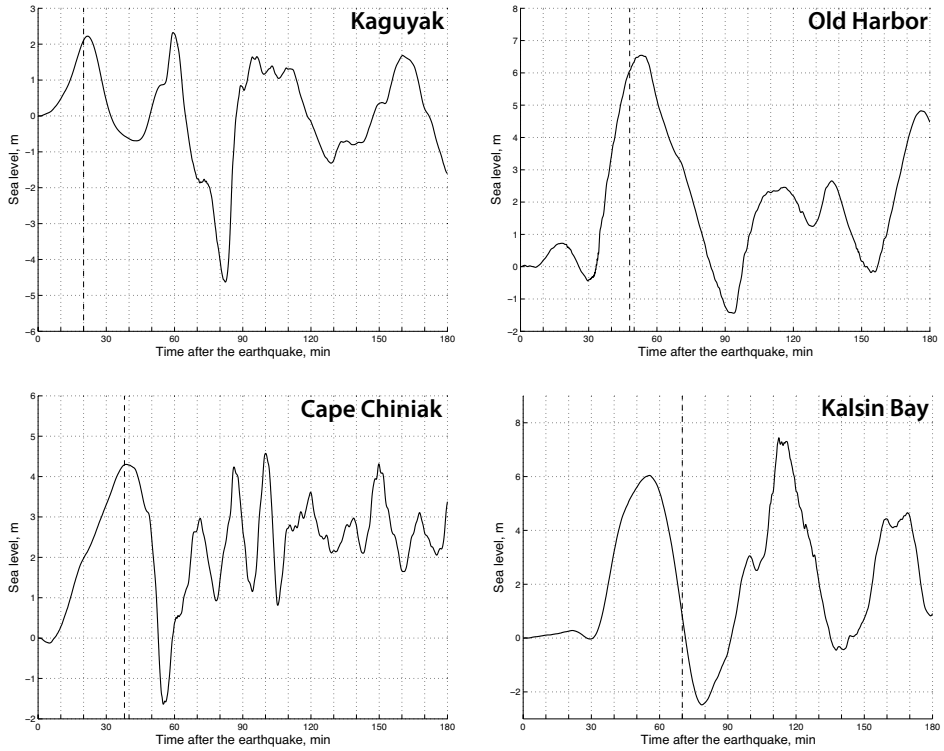

Figure 13. Simulated time series of tsunami waves at 4 locations on Kodiak Island. The initial conditions correspond to the deformation model shown in Figure 11. Dashed line on each graph indicates arrival of the first wave crest.

Kalsin Bay. This point is in the 3-arc-second grid, where the resolution of the grid is about 44m x 82m. The time series point is located in deep water near the head of the bay. The calculated arrival is 55 minutes after the earthquake. This is one of only 3 locations on the island where arrival times and runup heights were recorded instrumentally by USGS streamflow gauges (Plafker & Kachadoorian, 1966). In Kalsin Bay, the gauge was situated at a site near the mouth of Myrtle Creek, where the creek intersects with the Chiniak Highway. The elevation of this point is about 15 meters, and it subsided during the earthquake by about 1.5 meters. Obviously, it subsided enough to bring it within reach of the highest tsunami waves, but at the same time it was still too high to record astronomical tides after the earthquake, unlike the two other streamflow gauges on the Shelikof Strait side of the island (Plafker & Kachadoorian, 1966). The Myrtle Creek gauge data show that the first wave arrived at the gauge about 70 minutes after the earthquake, or about 15 minutes after the calculated arrival of this wave into the bay (Figure 13d). There are several possible explanations for this discrepancy. First we need to mention that the calculated arrival time of 55 minutes seems logical, given that the first wave arrival in Kalsin Bay was the same wave that hit Cape Chiniak at 38 minutes after the earthquake and then, refracting around the Cape, first arrived to Kalsin Bay, and then was recorded with a high degree of accuracy at Naval Station at 63 minutes after the earthquake. Second, the deeper than actual depths within Kalsin Bay used in the model could make the wave arrive sooner at the gauge location, since travel time strongly depends on water depth, and the bathymetry data in the 3-arc-second grid are not of high accuracy. Third, it takes some time for a wave to inundate dry land at elevation of about 15 meters, since friction effects start playing a more significant role. In order to calculate inundation of dry land and runup heights within Kalsin Bay, a good quality high-resolution grid of combined bathymetry and topography would be required.

Kodiak Naval Station. This is the only location along the Gulf of Alaska coast that has a complete and reliable record of tsunami waves (Kachadoorian & Plafker, 1969). Personnel of the Fleet Weather Central at the Kodiak Naval Station kept a log of arriving waves. The calculated time series at the Kodiak Naval Station is shown in Figure 14. The arrows indicate observed arrivals of the first 5 waves. The modeling results are in good agreement with observations. The model was even able to reproduce the third bifurcated wave, which means that the distribution of slip in the fault model of Kodiak asperity produced the reasonable initial displacements of the ocean bottom throughout the region. Since the slip distribution pattern and therefore the coseismic displacements are very complex, visualization of the animated tsunami wave field is a good tool to analyze arrivals of waves and their sources in the rupture area. The animated tsunami propagation (Movie S1) shows that the first crest at the Naval Station originated in the area of high slip in the Kodiak asperity indicated by letter "B" in Figure 11. This wave first hits the coastline between Cape Chiniak and Narrow Cape, and then refracts around Cape Chiniak and enters Chiniak Bay (Figures 1 and 12b). The secondary crest forms in the same area of high slip offshore south-eastern part of Kodiak Island and arrives to the Naval Station an hour later. Our results show that our updated source function provides a good match to the observations, and much better than does the model used in Suleimani et al. (2003).

Kodiak City. Although both Kodiak City and the Kodiak Naval Station are in St. Paul Harbor, separated only by 8 km along the coast (Figure 12b), the wave histories were different at these two locations. The waves were arriving mostly from the southeast at the Naval Station, which is an open location on the coast, and is sheltered from the north-east waves by Woody Island and Near Island. At Kodiak City the wave pattern was more complicated due to interference of waves arriving from 2 major directions - from the southeast and from the northeast, through the channel that separates downtown Kodiak and Near Island (Figure 12b). Very few eyewitness accounts exist for the reconstruction of wave history in Kodiak City (Kachadoorian & Plafker, 1969), because of the timely tsunami warning that prompted local residents to evacuate to higher ground,

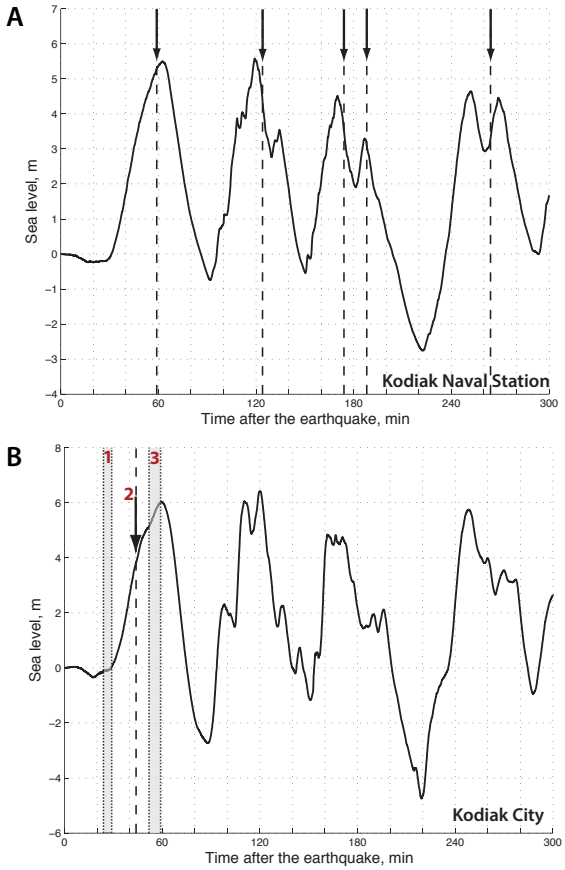

Figure 14. Simulated time series of tsunami waves at the Kodiak Naval Station (A) and at the City of Kodiak (B). The initial conditions correspond to the deformation model shown in Figure 11. The arrows in the upper plot indicate the documented arrivals of the first five waves at the Naval Station. Numbers 1, 2 and 3 in the lower plot show observed arrivals of the first 3 waves in the City of Kodiak. The shaded areas indicate that the arrival time was within that interval.

and the arrival times are only estimates (Kachadoorian & Plafker, 1969). The calculated time series at Kodiak City (Figure 14b) resembles the time series at the Naval Station, with waves arriving at about the same intervals. This result seems logical, since these two locations are very close to each other, and the arriving tsunami waves are long-period waves. However, the eyewitnesses reported two more waves at Kodiak City (marked by A and B) before the arrival of the third wave that was the first recorded at the Naval Station 63 minutes after the earthquake. These two waves arrived from the northeast through the channel that separates Kodiak City from Near Island (Figure 12b). The resolution of the numerical grid is not high enough to adequately represent the narrow channel and interference of northeastern waves with the waves that arrived from southeast.

The analysis of calculated tsunami time series at several locations along the southeastern shore of Kodiak Island shows that the updated coseismic source function produces tsunami arrivals that agree well with the observations. This result suggests that the updated coseismic deformation model provides a good estimate of slip in the Kodiak asperity.

5 Discussion and Conclusions

We performed a near-field numerical study of the source of tsunami waves generated by the M_{w}9.2 1964 Alaska earthquake. First, the older deformation models by Johnson et al. (1996) and Ichinose et al. (2007) generated very different tsunami wave fields in the rupture area of the 1964 earthquake and produced tsunami arrival times and amplitudes that did not agree with the near-field observations, but the model of Suito and Freymueller (2009) matches these well, even though tsunami arrivals were not specifically considered in the development of that model. We therefore used the most recent coseismic slip model of Suito and Freymueller (2009) as the basis for the new, modified source function of the 1964 tsunami.

We investigated the effect of secondary intraplate (splay) faults on local tsunami waves. Our results support the observations that splay faulting extended farther than the mapped dimensions of the Patton Bay fault (Plafker, 1967; Liberty et al., 2019). We corrected an error in Suito and Freymueller (2009) in the position of the splay fault line with respect to the Montague Island coast in the fault geometry, and used the near-field tsunami modeling results, observations of the tsunami arrival times and polarity of first arrivals to constrain the fault length along the southern coast of the Kenai Peninsula. We find that the splay fault is longer than that in the coseismic models of Holdahl and Sauber (1994), Johnson et al. (1996) and Ichinose et al. (2007) and extends beyond the region currently mapped by Liberty et al. (2019), but does not reach the western tip of the Kenai Peninsula, as proposed in the original model by Suito and Freymueller (2009).

Our proposed extent of the fault to about 150°W approximately corresponds to the edge of the large area of interseismic slip deficit associated with the Prince William Sound asperity (Suito & Freymueller, 2009; Li et al., 2016). In the coseismic model, this boundary also corresponds to the disconnect between the splay fault and the megathrust. We confirm that inclusion of the splay fault into the source function has little effect on the tsunami in the far field (Johnson et al., 1996). This supports the proposal by Liberty et al. (2019) that the active splay fault extent is intrinsically connected to the extent of the Prince William Sound asperity, and that the asperity is persistent.

We found that the horizontal displacements had a pronounced effect on the far-field tsunami, with a 10 to 18% increase in wave amplitudes of the first arrival at several locations on the US west coast. A comparable effect could result from inclusion of the kinetic energy term. The horizontal displacements have a much smaller effect in the near field, about 7-8%, except in a few specific areas. The area of maximum vertical deformation due to horizontal displacements was in the Kodiak asperity and directed tsunami

energy toward the eastern coast of Kodiak Island, where maximum runup was observed. Another local deformation maximum increased tsunami amplitudes along the short section of the southern coast of the Kenai Peninsula.

Analysis of tsunami impact on the southeastern shore of Kodiak Island confirmed that the Kodiak asperity was an important and robust feature of the 1964 rupture (Christensen & Beck, 1994; Holdahl & Sauber, 1994; Johnson et al., 1996; Ichinose et al., 2007). The Suito and Freymueller (2009) coseismic slip model provides a good estimate of slip in the Kodiak asperity. Along the south coast of Kodiak, coseismic slip on the megathrust alone is capable of producing the tsunami arrivals and amplitudes that agree well with the observations, and there is no evidence for splay faulting off of the Kodiak shore in 1964. We were not able to utilize the runup measurements along this coastline due to absence of combined bathymetry and topography data sets for calculation of runup.

Accounting for the initial ocean surface uplift due to horizontal motion of the bottom increases the amplitudes of the first arrivals in the far field, while the splay fault affects the waveforms later during the tsunami propagation span. Both source features have effects in the near field, but in different locations. While the displacements on the splay fault have very strong effects on the tsunami arrivals, amplitude and inundation at the Kenai Peninsula sites, the horizontal bottom motion influences tsunami wave field mostly in the Kodiak region.

When analyzing results of numerical modeling and comparing them with observations, we need to mention several limitations of the model. One of them is that the model accounts only for the static vertical deformation of the ocean surface that results from vertical and horizontal displacements on the fault. The other component, which is transfer of kinetic energy from a horizontally moving bottom slope into the water column, cannot be simulated in the current model formulation. Accounting for this transfer of energy directed toward the west coast of the United States would result in increase of tsunami amplitudes by 20% or more, which so far have been underestimated in all previous modeling studies. Also, the model does not take into account the effects of propagating rupture, using only the static coseismic deformation of the seafloor. For earthquakes with extremely long rupture zones, such as the 1964 Alaska and 2004 Sumatra earthquakes, modeling the dynamic rupture could introduce corrections into the near-field tsunami arrival times and amplitudes. Song et al. (2008) suggested that the effects of propagating rupture and kinetic energy transfer can be combined by applying 3-D earthquake forcing to the ocean model during the rupture period or the tsunami initialization period. The use of the near-field runup data was limited in this source function study due to lack of high-resolution combined bathymetry and topography DEMs in coastal locations where runup measurements were carried out. Also, at many places the highest runup was not caused by the first wave, but resulted from one of the later arrivals, which coincided with high tide and could have been amplified by interactions of tsunami waves and tides. In order to make use of those runup observations, nonlinear tsunami-tide interactions would need to be included into the model.

Acknowledgments

This publication is the result in part of research sponsored by the Cooperative Institute for Alaska Research (CIFAR) with funds from the National Oceanic and Atmospheric Administration (NOAA) under cooperative agreement NA08OAR4320751 with the University of Alaska. Numerical calculations for this work are supported by a grant of High Performance Computing resources from the Arctic Region Supercomputing Center at the University of Alaska Fairbanks as part of the US Department of Defense HPC Modernization Program. We are grateful to Dr. Dmitry Nicolsky for development of the Alaska Tsunami Online Mapping interface that we used for multiple model runs and for the analysis of the results. We are thankful to Dr. George Plafker for his compilations of the 1964

runup data and for insightful discussions. We also thank Rod Combellick and Keith Labay for providing us with digitized coordinates of nodes along the Patton Bay fault.

The near-field tsunami observations summarized in Table 1 were extracted from published reports as cited. The low resolution seafloor bathymetry was taken from ETOPO2 (https://sos.noaa.gov/datasets/etopo2-topography-and-bathymetry-natural-colors/), while the higher resolution grids are available at NOAA's National Centers for Environmental Information (https://www.ngdc.noaa.gov/mgg/coastal/). The modified source function, a gridded version of its displacement predictions, and simulated tsunami models will be archived at a data center to be determined before the time of final paper acceptance.

References

Ben-Menahem, A., & Rosenman, M. (1972). Amplitude patterns of tsunami waves from submarine earthquakes. *J. Geophys. Res.*, *77*(17), 3097–3128. doi: 10.1029/JB077i017p03097

Carver, G., & Plafker, G. (2008). Paloseismicity and neotectonics of the Aleutian subduction zone - an overview. In J. Freymueller, P. Haeussler, R. Wesson, & G. Ekström (Eds.), *Acive tectonics and seismic potential of Alaska* (pp. 43–63). Washington, DC: AGU.

Christensen, D., & Beck, S. (1994). The rupture process and tectonic implications of the Great 1964 Prince William Sound earthquake. *Pure Appl. Geophys.*, *142*(1), 29–53.

Coulter, H., & Migliaccio, R. (1966). *Effects of the Earthquake of March 27, 1964, at Valdez, Alaska.* U.S. Geological Survey Professional Paper 542-C, 36 pp.

Emore, G. L., Haase, J. S., Choi, K., Larson, K. M., & Yamagiwa, A. (2007). Recovering seismic displacements through combined use of 1-hz gps and strong-motion accelerometers. *Bull. Seism. Soc. Am.*, *97*(2), 357-378. doi: 10.1785/0120060153

Heidarzadeh, M., Muhari, A., & Wijanarto, A. B. (2019, Jan 01). Insights on the source of the 28 September 2018 Sulawesi tsunami, Indonesia based on spectral analyses and numerical simulations. *Pure and Applied Geophysics*, *176*(1), 25–43. Retrieved from `https://doi.org/10.1007/s00024-018-2065-9` doi: 10.1007/s00024-018-2065-9

Holdahl, S., & Sauber, J. (1994). Coseismic slip in the 1964 Prince William Sound earthquake: A new geodetic inversion. *Pure Appl. Geophys.*, *142*, 55–82.

Ichinose, G., Somerville, P., Thio, H., Graves, R., & O'Connell, D. (2007). Rupture process of the 1964 Prince William Sound, Alaska, earthquake from the combined inversion of seismic, tsunami, and geodetic data. *J. Geophys. Res.*, *112*(B07306).

Jamelot, A., Gailler, A., Heinrich, P., Vallage, A., & Champenois, J. (2019, Aug 01). Tsunami simulations of the Sulawesi $M_{\mathrm{W}}7.5$ event: Comparison of seismic sources issued from a tsunami warning context versus post-event finite source. *Pure and Applied Geophysics*, *176*(8), 3351–3376. Retrieved from `https://doi.org/10.1007/s00024-019-02274-5` doi: 10.1007/s00024-019-02274-5

Johnson, J., Satake, K., Holdahl, S. R., & Sauber, J. (1996). The 1964 Prince William Sound earthquake: Joint inversion of tsunami and geodetic data. *J. Geophys. Res.*, *101*, 523-532.

Kachadoorian, R. (1965). *Effects of the earthquake of March 27, 1964 at Whittier, Alaska.* U.S. Geological Survey Professional Paper 542-B, 21 pp.

Kachadoorian, R., & Plafker, G. (1967). *Effects of the earthquake of March 27, 1964 on the communities of Kodiak and nearby islands.* U.S. Geological Survey Professional Paper 542-F, 41 pp.

Kachadoorian, R., & Plafker, G. (1969). *Effects of the Earthquake of March 27, 1964 on the communities of Kodiak and nearby islands.* U.S. Geological Survey Professional Paper 542-F, 41 pp.

Lander, J. (1996). *Tsunamis affecting Alaska. 1737–1996* (No. 31). Boulder, Colo.: National Geophysical Data Center.

Lay, T., Kanamori, H., Ammon, C. J., Nettles, M., Ward, S. N., Aster, R. C., ... Sipkin, S. (2005). The Great Sumatra-Andaman Earthquake of 26 December 2004. *Science*, *308*(5725), 1127-1133. doi: 10.1126/science.1112250

Lemke, R. (1967). *Effects of the Earthquake of March 27, 1964, at Seward, Alaska.* U.S. Geological Survey Professional Paper 542-E, 48 pp.

Li, S., Freymueller, J., & McCaffrey, R. (2016). Slow slip events and time-dependent variations in locking beneath Lower Cook Inlet of the Alaska-Aleutian subduction zone. *Journal of Geophysical Research: Solid Earth*, *121*. doi: doi:10.1002/2015JB012491

Liberty, L. M., Brothers, D. S., & Haeussler, P. J. (2019). Tsunamigenic splay faults imply a long-term asperity in southern Prince William Sound, Alaska. *Geophysical Research Letters*, *46*(7), 3764-3772. Retrieved from `https://agupubs.onlinelibrary.wiley.com/doi/abs/10.1029/2018GL081528` doi: 10.1029/2018GL081528

Liberty, L. M., Finn, S. P., Haeussler, P. J., Pratt, T. L., & Peterson, A. (2013). Megathrust splay faults at the focus of the Prince William Sound asperity, Alaska. *Journal of Geophysical Research: Solid Earth*, *118*(10), 5428-5441. Retrieved from `https://agupubs.onlinelibrary.wiley.com/doi/abs/10.1002/jgrb.50372` doi: 10.1002/jgrb.50372

Malloy, R., & Merrill, G. (1972). Vertical crustal movement on the sea floor. In *The Great Alaska Earthquake of 1964. oceanography and Coastal Engineering* (pp. 252–265). National Academy of Sciences, Washington, D.C.

Nicolsky, D., Suleimani, E., & Hansen, R. (2010). Validation and verification of a numerical model for tsunami propagation and runup. *Pure Appl. Geophys.*. doi: 10.1007/s00024-010-0231-9

Nishenko, S., & Jacob, K. (1990). Seismic potential of the Queen Charlotte-Alaska-Aleutian seismic zone. *J. Geophys. Res.*, *95*(B3), 2511-2532.

Okada, Y. (1985). Surface deformation due to shear and tensile faults in a half-space. *Bull. Seism. Soc. Am.*, *75*, 1135–1154.

Plafker, G. (1967). *Surface faults on Montague Island associated with the 1964 Alaska Earthquake.* U.S. Geological Survey Professional Paper 543-G, 42 pp.

Plafker, G. (1969). *Tectonics of the March 27, 1964 Alaska Earthquake.* U.S. Geological Survey Professional Paper 543-I, 74 pp.

Plafker, G. (2006). *The great 1964 Alaska Earthquake as a model for tsunami generation during megathrust earthquakes with examples form Chile and Sumatra.* Abstracts of the AGU Chapman Conference on the Active Tectonics and Seismic Potential of Alaska.

Plafker, G., & Kachadoorian, R. (1966). *Kodiak and Nearby Islands.* U.S. Geological Survey Professional Paper 543-D, 46 pp.

Plafker, G., Kachadoorian, R., Eckel, E., & Mayo, L. (1969). *Effects of the Earthquake of March 27, 1964 on various communities.* U.S. Geological Survey Professional Paper 542-G, 50 pp.

Santini, S., Dragoni, M., & Spada, G. (2003). Asperity distribution of the 1964 Great Alaska earthquake and its relation to subsequent seismicity in the region. *Tectonophysics*, *367*, 219–233. doi: 10.1016/S0040-1951(03)00130-6

Song, Y., Fu, L., Zlotnicki, V., Ji, C., Hjorleifsdottir, V., Shum, C., & Yi, Y. (2008). The role of horizontal impulses of the faulting continental slope in generating the 26 December 2004 tsunami. *Ocean Modelling*, *20*, 362–379. doi: 10.1016/j.ocemod.2007.10.007

Spaeth, M., & Berkman, S. (1972). Tsunami of March 28, 1964, as recorded at tide

stations and the Seismic Sea Waves Warning System. In *The Great Alaska Earthquake of 1964. oceanography and Coastal Engineering* (p. 38-100). National Academy of Sciences, Washington, D.C.

Suito, H., & Freymueller, J. (2009). A viscoelastic and afterslip postseismic deformation model for the 1964 Alaska earthquake. *J. Geophys. Res.*, *114*(B11404). doi: 10.1029/2008JB005954

Suleimani, E. (2011). *Numerical studies of tectonic and landslide-generated tsunamis caused by the 1964 Great Alaska Earthquake* (Unpublished doctoral dissertation). University of Alaska Fairbanks, Fairbanks, Alaska. (181 pp.)

Suleimani, E., Hansen, R., & Kowalik, Z. (2003). Inundation modeling of the 1964 tsunami in Kodiak Island, Alaska. In A. Yalciner, E. Pelinovsky, E. Okal, & C. Synolakis (Eds.), *Submarine Landslides and Tsunamis, NATO Science Series, Series IV: Earth and Environmental Sciences, vol. 21* (pp. 191–201). Kluwer Academic Publishers.

Suleimani, E., Nicolsky, D., Haeussler, P., & Hansen, R. (2010). Combined effects of tectonic and landslide-generated tsunami runup at Seward, Alaska, during the M_{W}9.2 1964 earthquake. *Pure Appl. Geophys.*. doi: 10.1007/s00024-010-0228-4

Synolakis, C., Bernard, E., Titov, V., Kânoğlu, U., & González, F. (2007). *Standards, criteria, and procedures for NOAA evaluation of tsunami numerical models* (NOAA Tech. Memo. OAR PMEL-135, NTIS: PB2007-109601). Seattle, WA: NOAA/Pacific Marine Environmental Laboratory. (55 pp.)

Synolakis, C., Bernard, E., Titov, V., Kânoğlu, U., & González, F. (2008). Validation and verification of tsunami numerical models. *Pure Appl. Geophys.*, *165*, 2197–2228.

Tanioka, Y., & Satake, K. (1996). Tsunami generation by horizontal displacement of ocean bottom. *Geophys. Res. Lett.*, *23*(8), 861–864.

Tysdal, R., & Case, J. (1979). *Geologic map of the Seward and Blying Sound quadrangles, Alaska.* U.S. Geologic Survey Miscellaneous Investigation 1150, 12 p., 1 sheet, scale 1:250,000.

Ulrich, T., Vater, S., Madden, E. H., Behrens, J., van Dinther, Y., van Zelst, I., ... Gabriel, A.-A. (2019, Oct 01). Coupled, physics-based modeling reveals earthquake displacements are critical to the 2018 Palu, Sulawesi tsunami. *Pure and Applied Geophysics*, *176*(10), 4069–4109. Retrieved from `https://doi.org/10.1007/s00024-019-02290-5` doi: 10.1007/s00024-019-02290-5

Van Dorn, W. (1972). Source mechanism of the major tsunami. In *The Great Alaska Earthquake of 1964. Oceanography and Coastal Engineering* (p. 111-139). National Academy of Sciences, Washington, D.C.

Waller, R. (1966). *Effects of the Earthquake of March 27, 1964, in the Homer area, Alaska.* U.S. Geological Survey Professional Paper 542-D, 28 pp.

Wilson, B., & Tørum, A. (1968). *The tsunami of the Alaskan Earthquake, 1964: Engineering evaluation.* U.S. Army Corps of Engineers, Technical memorandum No. 25, 401 p.

Zweck, C., Freymueller, J., & Cohen, S. (2002). Three-dimensional elastic dislocaiton modeling of the postseismic response to the 1964 Alaska earthquake. *J. Geophys. Res.*, *107*(B4), 1–12.

Figure 1.

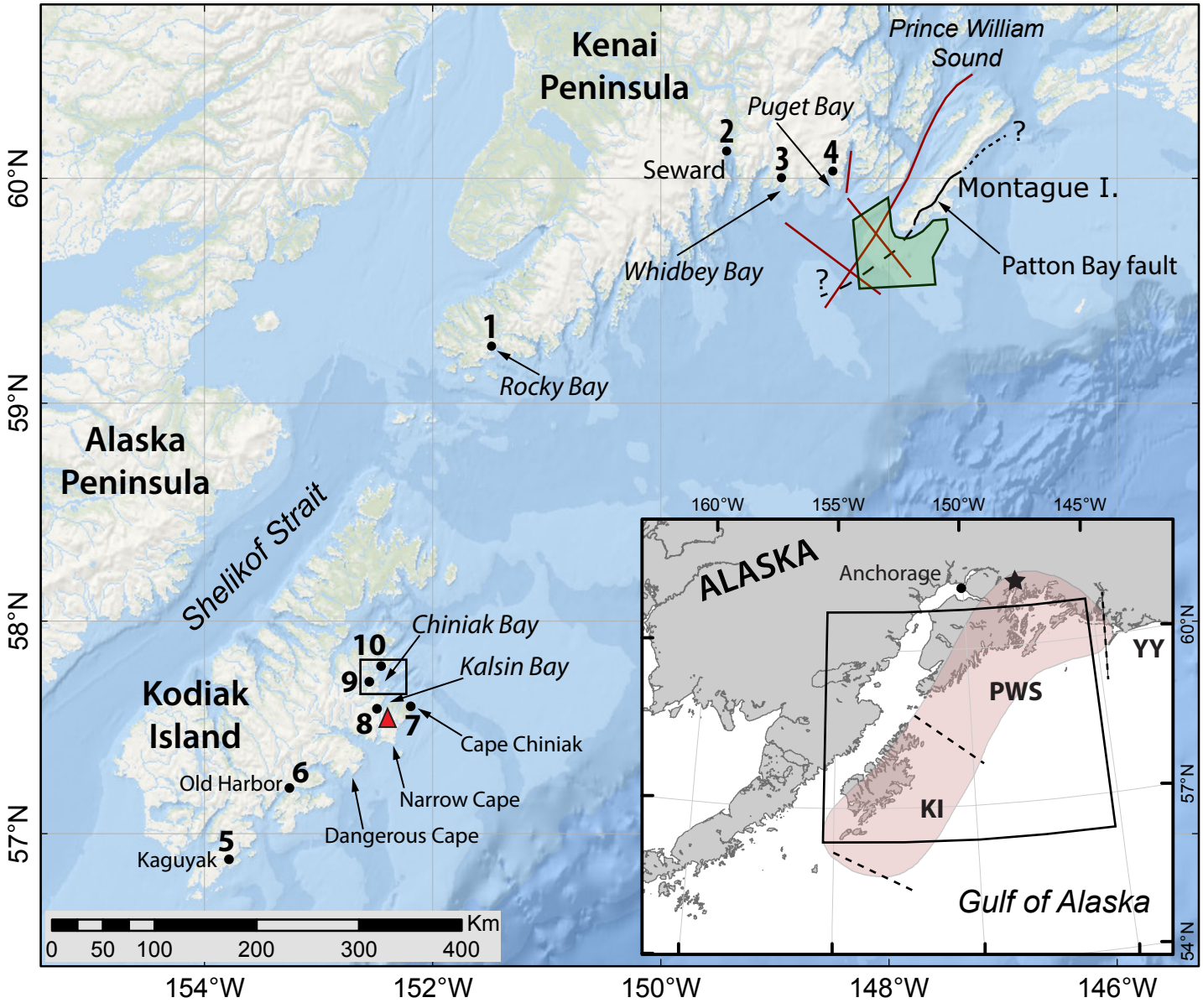
Kenai Peninsula
Prince William Sound
Puget Bay
Seward
2
3
4
Montague I.
Whidbey Bay
Patton Bay fault
1
Rocky Bay
Alaska Peninsula
Shelikof Strait
Chiniak Bay
10
9
Kalsin Bay
Kodiak Island
8
7
Cape Chiniak
Old Harbor
6
Narrow Cape
Dangerous Cape
5
Kaguyak
Km
0 50 100 200 300 400
60°N
59°N
58°N
57°N
154°W
152°W
150°W
148°W
146°W
160°W
155°W
150°W
145°W
ALASKA
Anchorage
YY
PWS
KI
Gulf of Alaska
60°N
57°N
54°N

Figure 2.

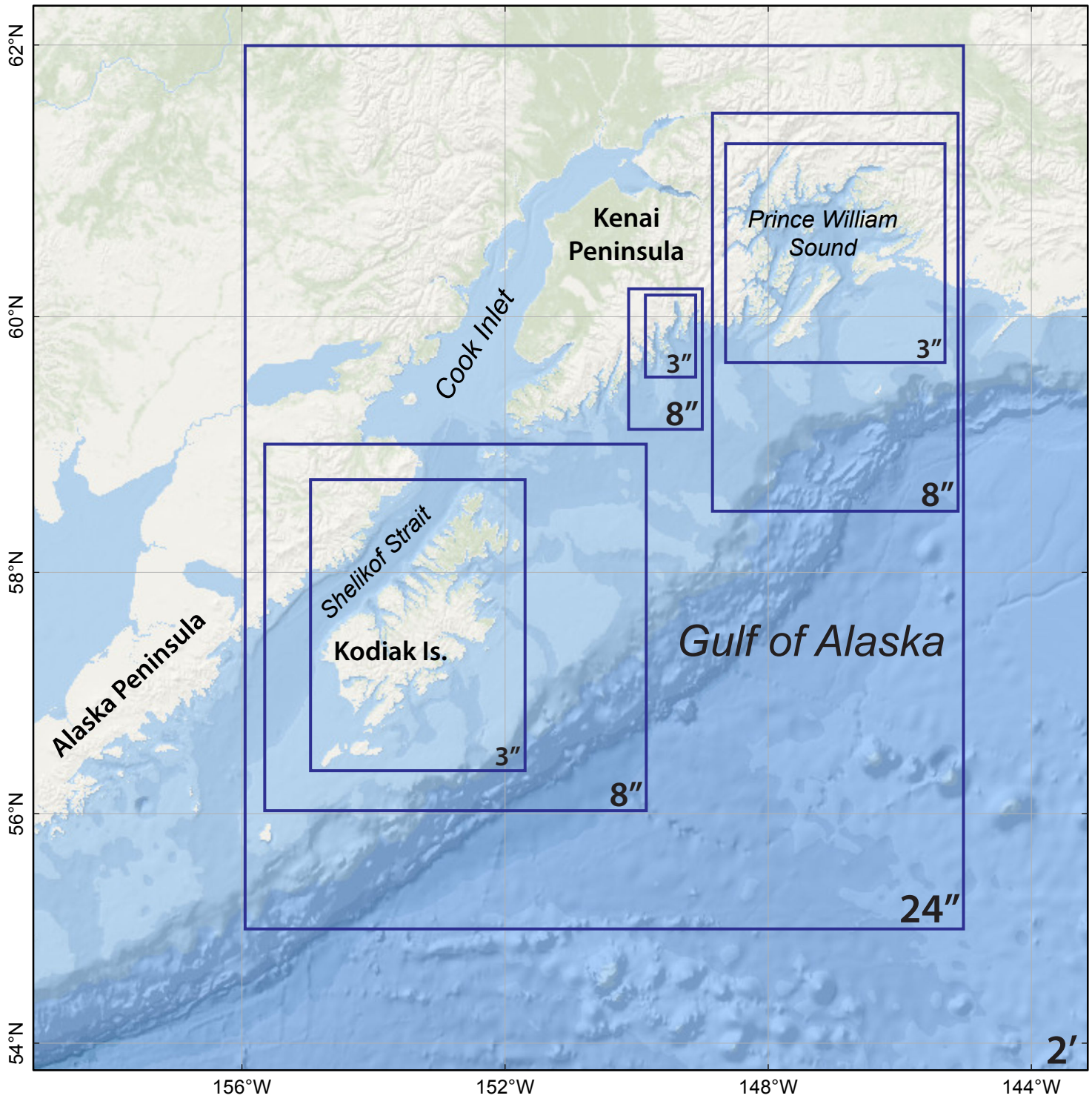
62°N
60°N
58°N
56°N
54°N
156°W
152°W
148°W
144°W
Kenai Peninsula
Cook Inlet
Prince William Sound
3″
8″
3″
8″
Shelikof Strait
Kodiak Is.
Alaska Peninsula
Gulf of Alaska
3″
8″
24″
2′

Figure 3.

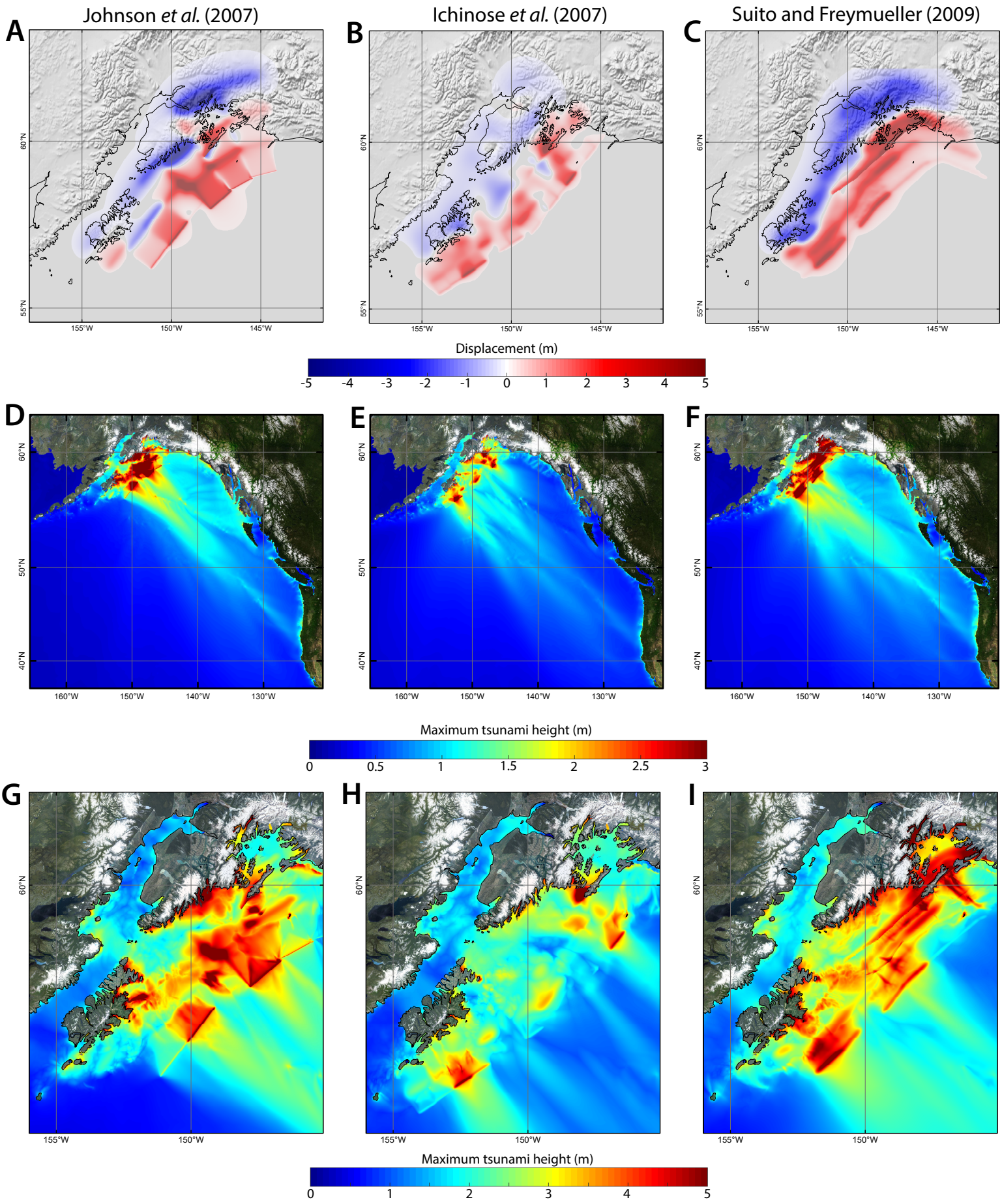
A
Johnson et al. (2007)
B
Ichinose et al. (2007)
C
Suito and Freymueller (2009)
60°N
55°N
155°W
150°W
145°W
Displacement (m)
-5
-4
-3
-2
-1
0
1
2
3
4
5
D
E
F
60°N
50°N
40°N
160°W
150°W
140°W
130°W
Maximum tsunami height (m)
0
0.5
1
1.5
2
2.5
3
G
H
I
60°N
155°W
150°W
Maximum tsunami height (m)
0
1
2
3
4
5

Figure 4.

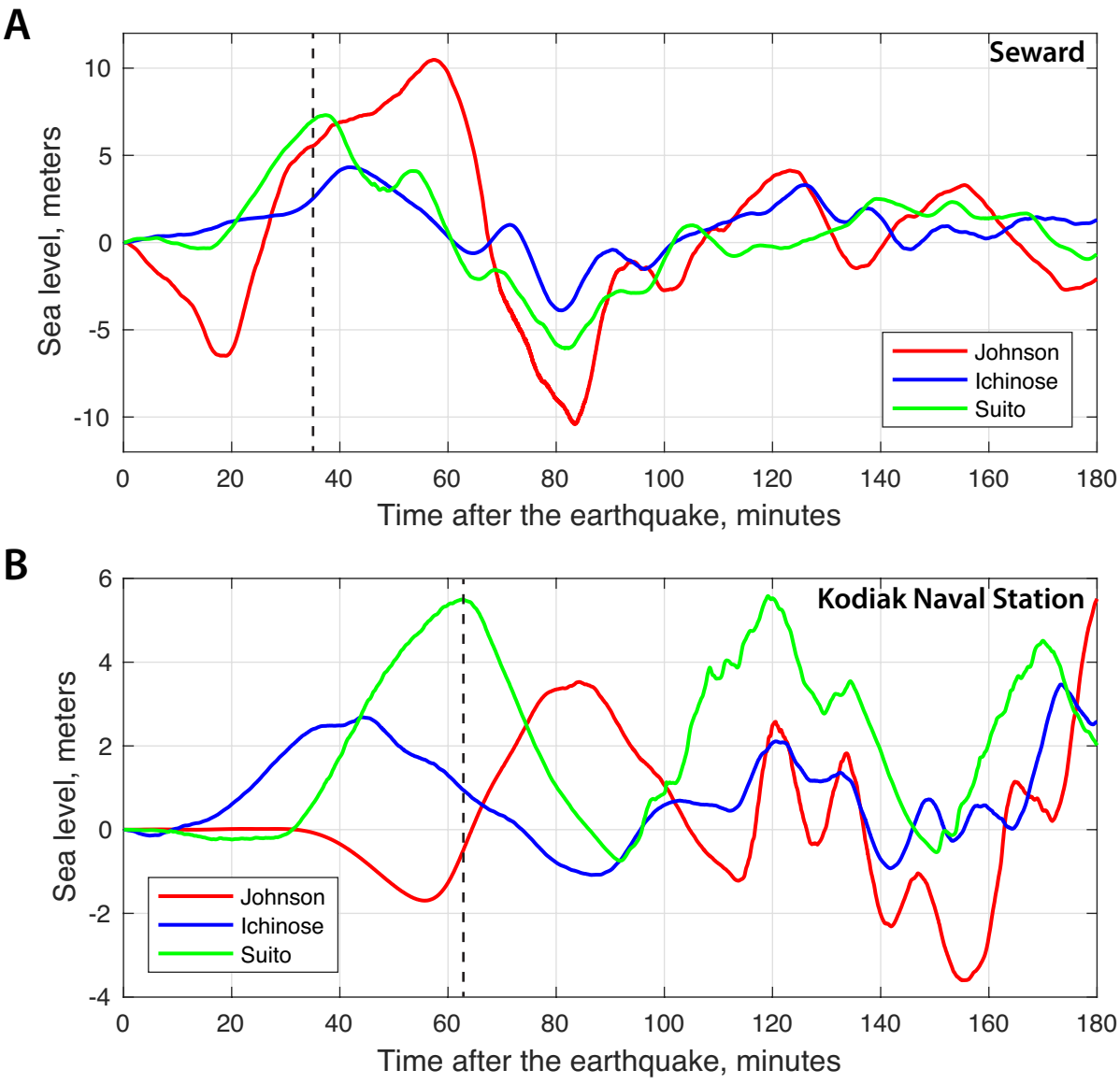
A
Seward
Sea level, meters
Time after the earthquake, minutes
Johnson
Ichinose
Suito
10
5
0
-5
-10
0
20
40
60
80
100
120
140
160
180

B
Kodiak Naval Station
Sea level, meters
Time after the earthquake, minutes
Johnson
Ichinose
Suito
6
4
2
0
-2
-4
0
20
40
60
80
100
120
140
160
180

Figure 5.

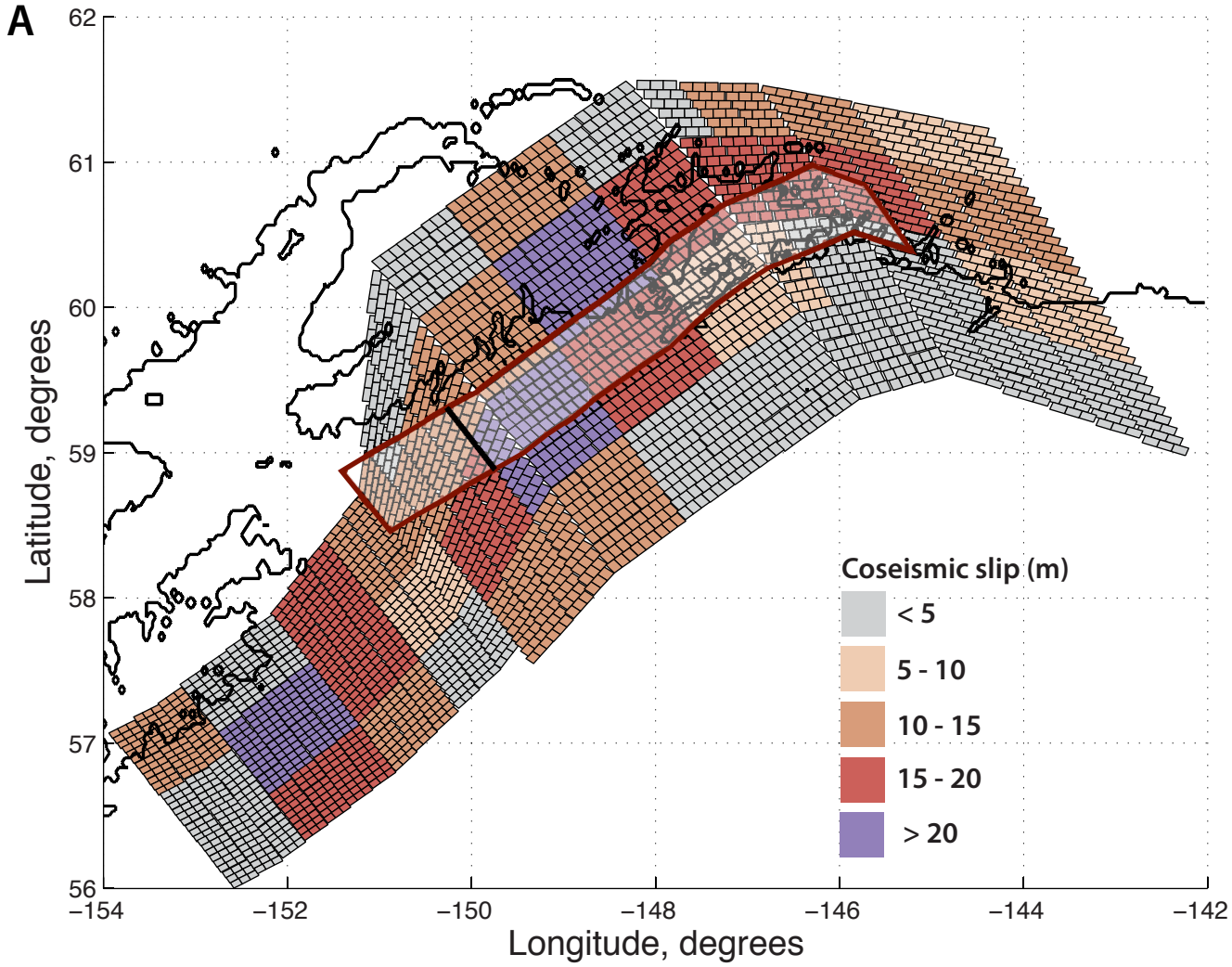
A
Latitude, degrees
Longitude, degrees
Coseismic slip (m)
< 5
5 - 10
10 - 15
15 - 20
> 20

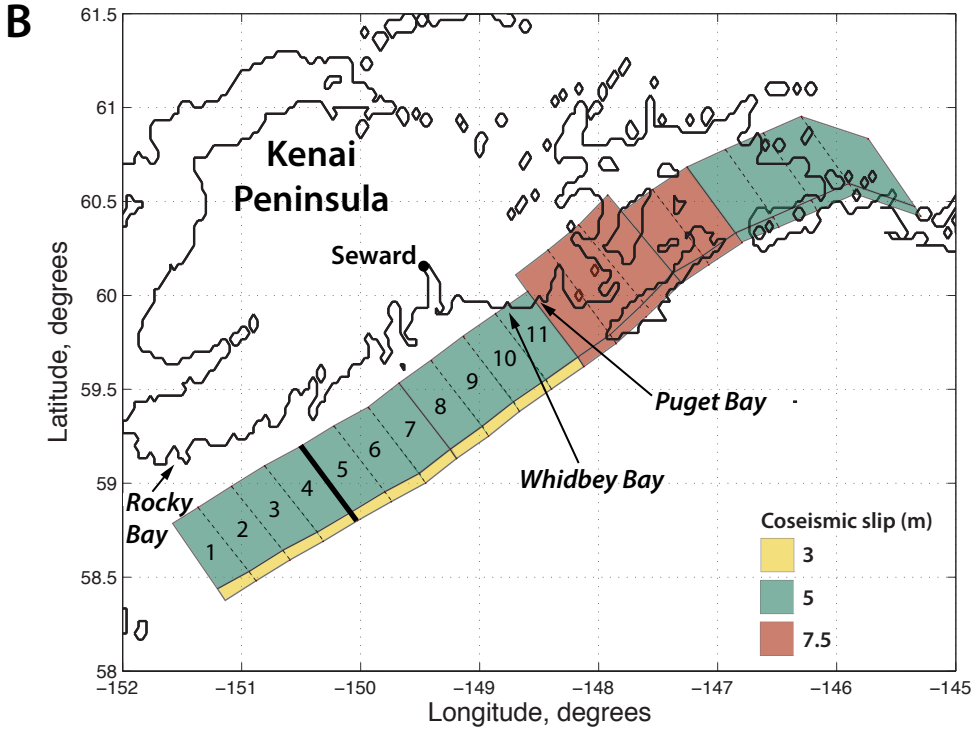
B
Kenai
Peninsula
Seward
Puget Bay
Whidbey Bay
Rocky
Bay
Latitude, degrees
Longitude, degrees
Coseismic slip (m)
3
5
7.5

Figure 6.

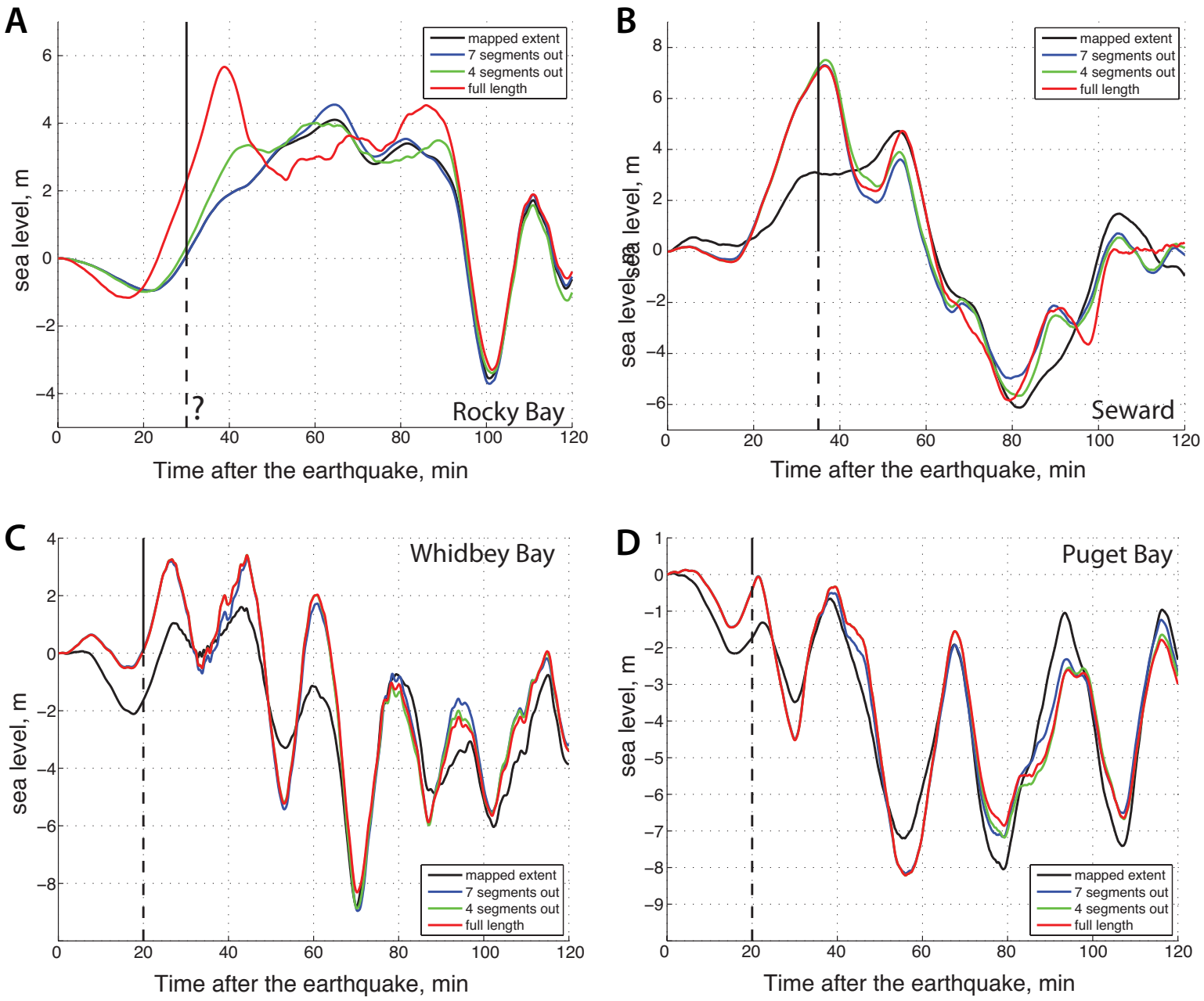
A
mapped extent
7 segments out
4 segments out
full length
sea level, m
?
Rocky Bay
Time after the earthquake, min
B
mapped extent
7 segments out
4 segments out
full length
sea level, m
Seward
Time after the earthquake, min
C
Whidbey Bay
sea level, m
mapped extent
7 segments out
4 segments out
full length
Time after the earthquake, min
D
Puget Bay
sea level, m
mapped extent
7 segments out
4 segments out
full length
Time after the earthquake, min

Figure 7.

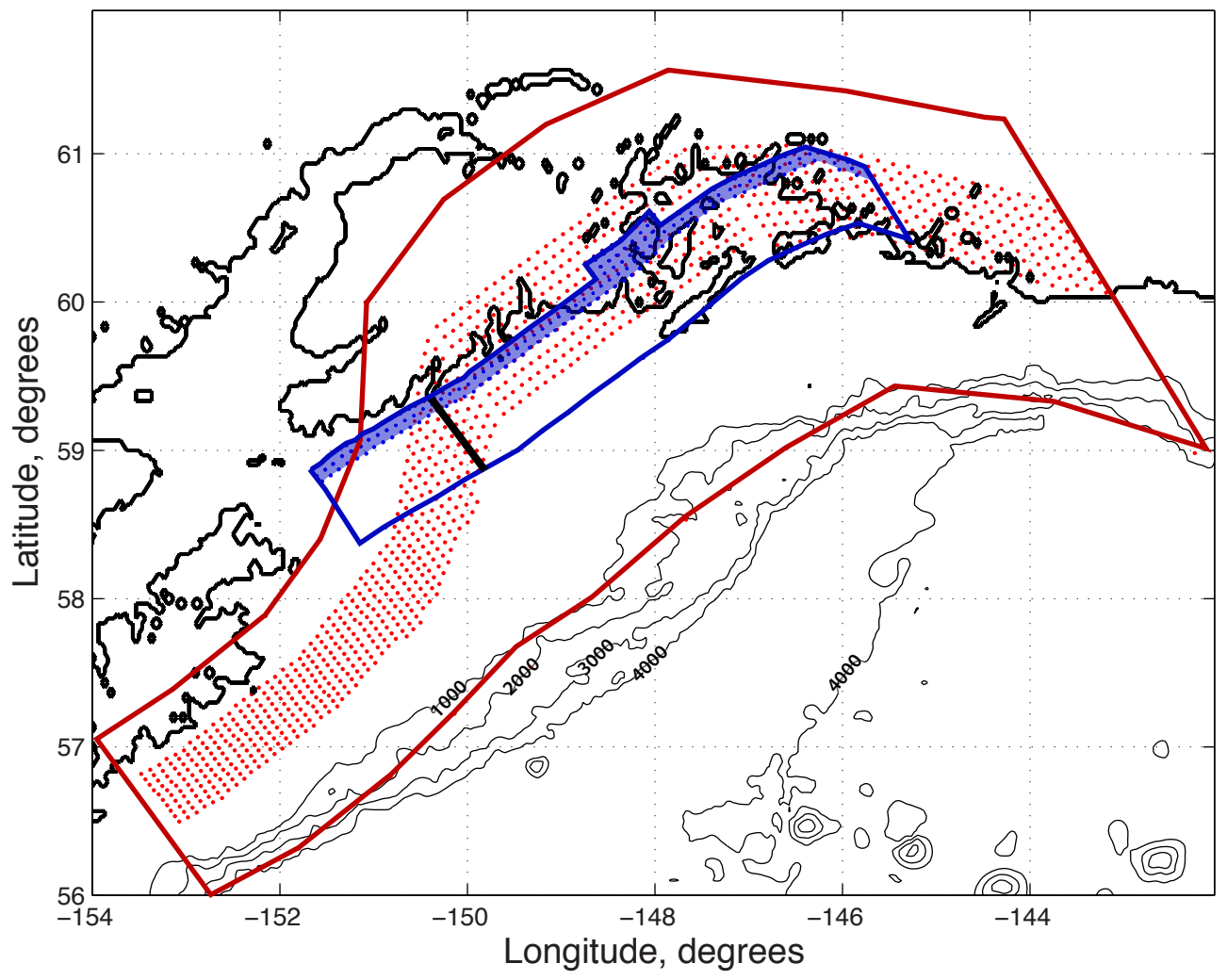
Latitude, degrees
Longitude, degrees
61
60
59
58
57
56
−154
−152
−150
−148
−146
−144
1000
2000
3000
4000
4000

Figure 8.

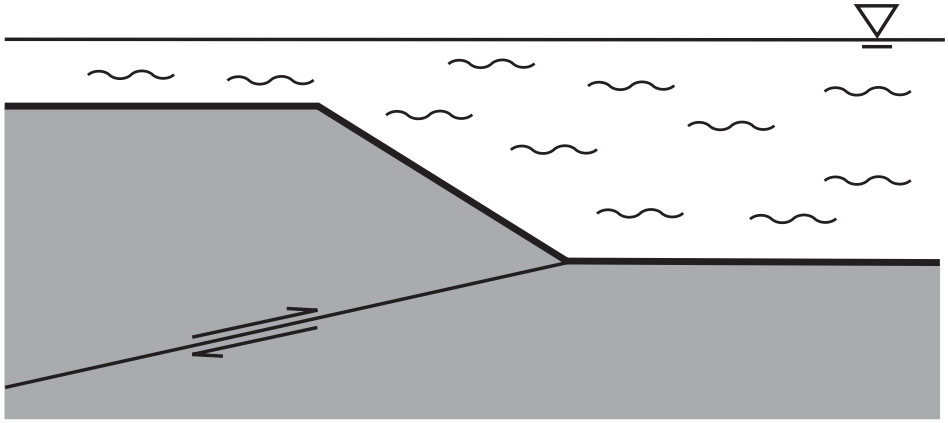

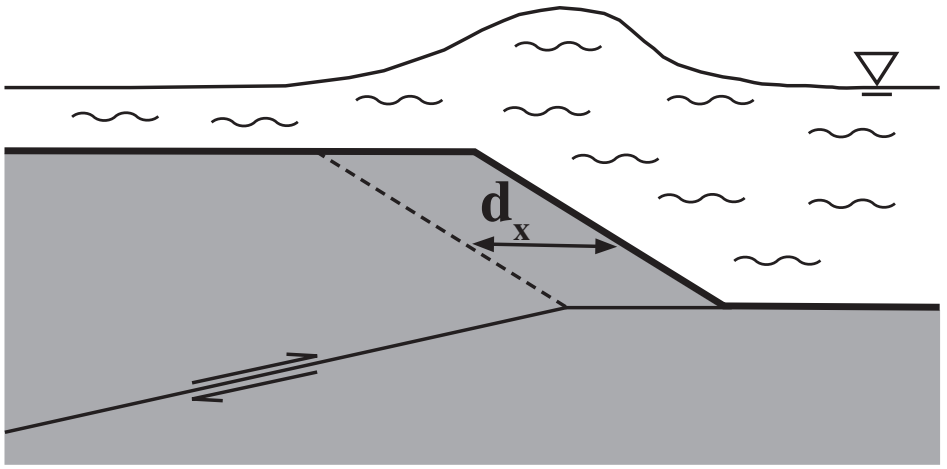
d_x

Figure 9.

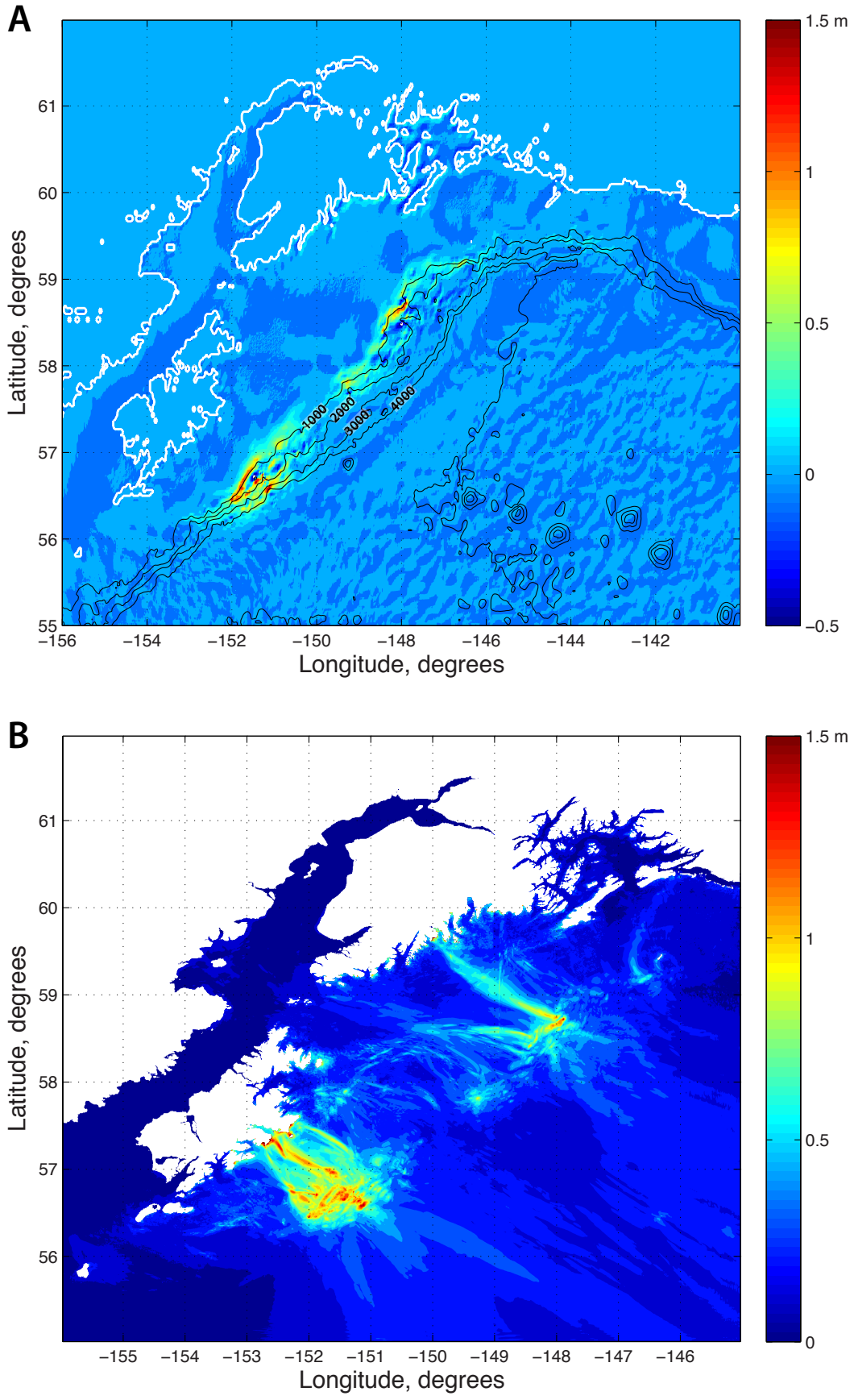
A
B
Latitude, degrees
Longitude, degrees
1.5 m
1
0.5
0
−0.5
1000
2000
3000
4000
55
56
57
58
59
60
61
−156
−154
−152
−150
−148
−146
−144
−142
−155
−153
−151
−149
−147
−145

Figure 10.

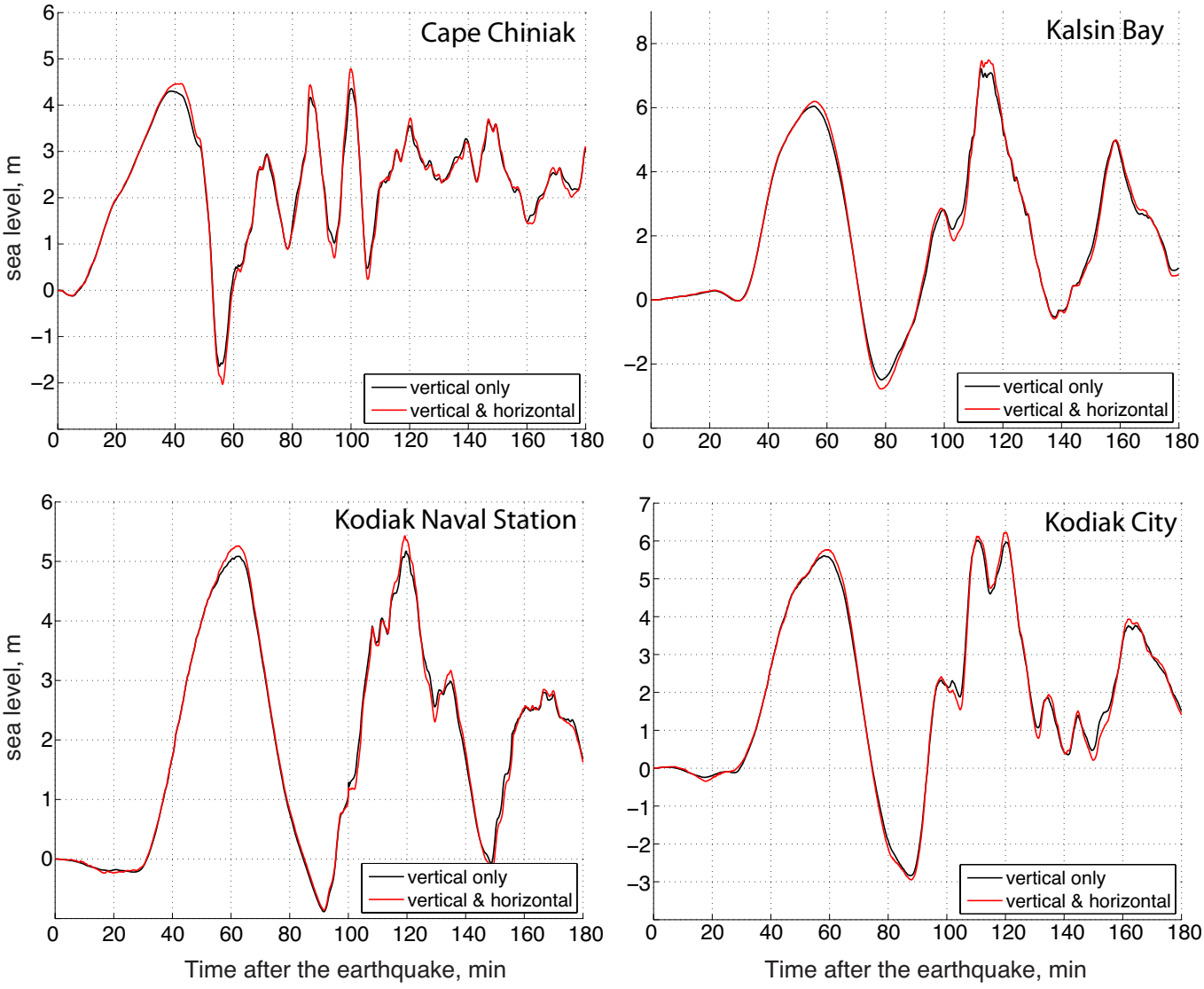
Cape Chiniak
Kalsin Bay
Kodiak Naval Station
Kodiak City
sea level, m
sea level, m
Time after the earthquake, min
Time after the earthquake, min
vertical only
vertical & horizontal
vertical only
vertical & horizontal
vertical only
vertical & horizontal
vertical only
vertical & horizontal

Figure 11.

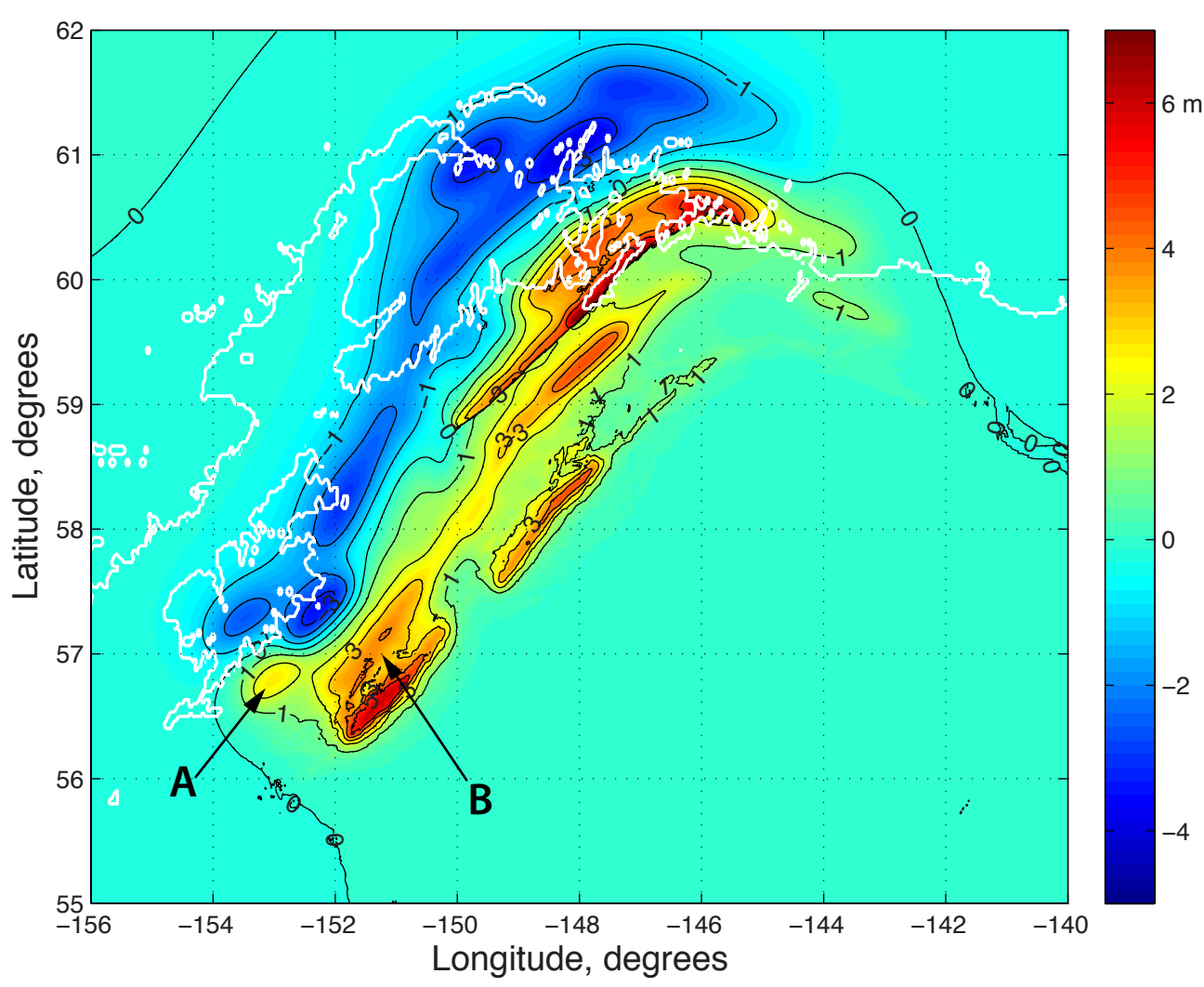
62
61
60
59
58
57
56
55
Latitude, degrees
−156
−154
−152
−150
−148
−146
−144
−142
−140
Longitude, degrees
6 m
4
2
0
−2
−4
A
B

Figure 12.

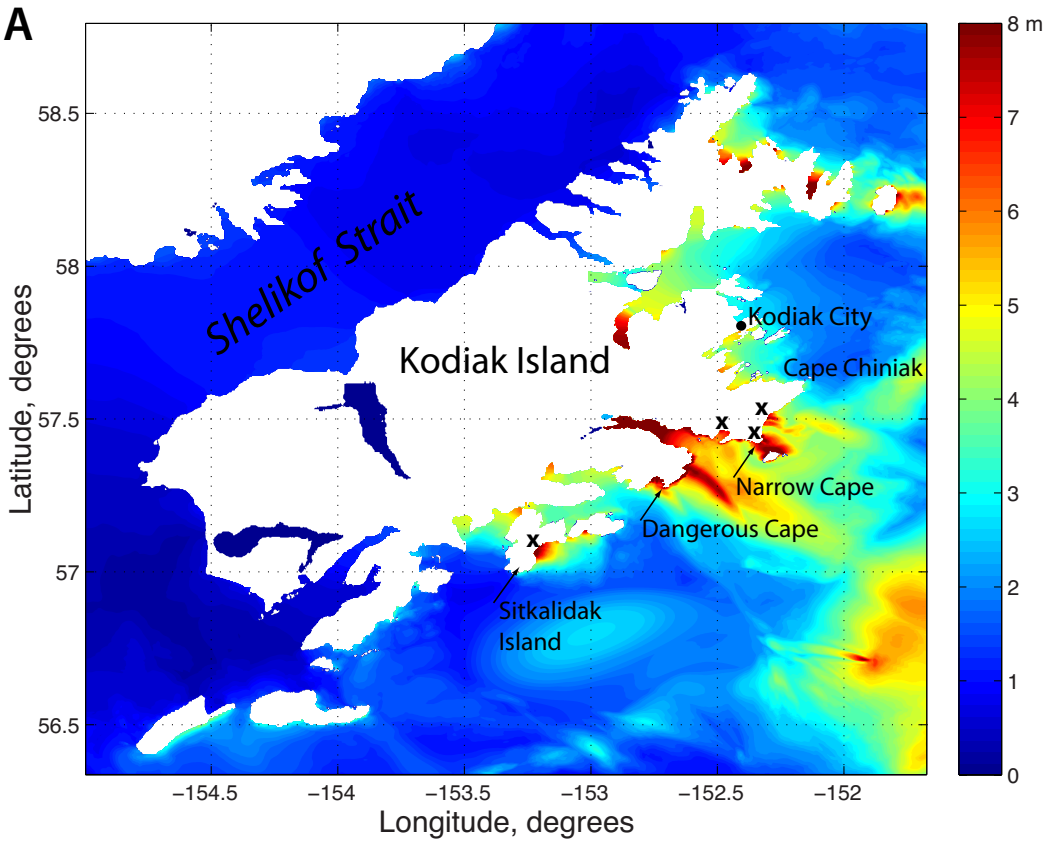
A
Shelikof Strait
Kodiak Island
Kodiak City
Cape Chiniak
Narrow Cape
Dangerous Cape
Sitkalidak Island
Latitude, degrees
Longitude, degrees
58.5
58
57.5
57
56.5
−154.5
−154
−153.5
−153
−152.5
−152
8 m
7
6
5
4
3
2
1
0


B
Kodiak City
Near I.
Woody I.
St. Paul Harbor
Kodiak Naval Station
Chiniak Bay

Figure 13.

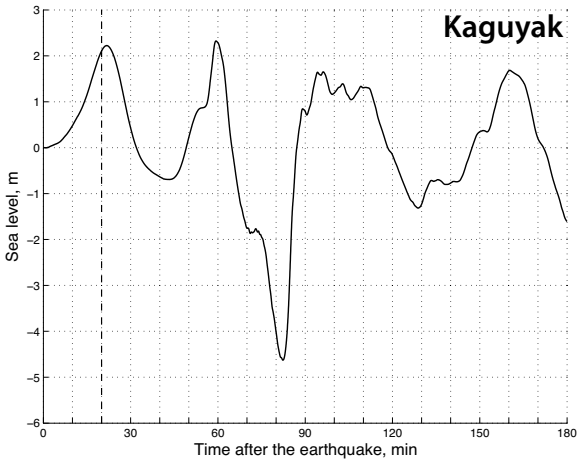
Kaguyak
Sea level, m
Time after the earthquake, min

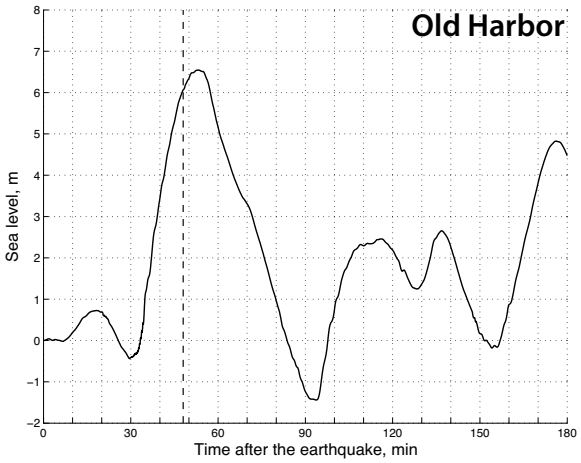
Old Harbor
Sea level, m
Time after the earthquake, min

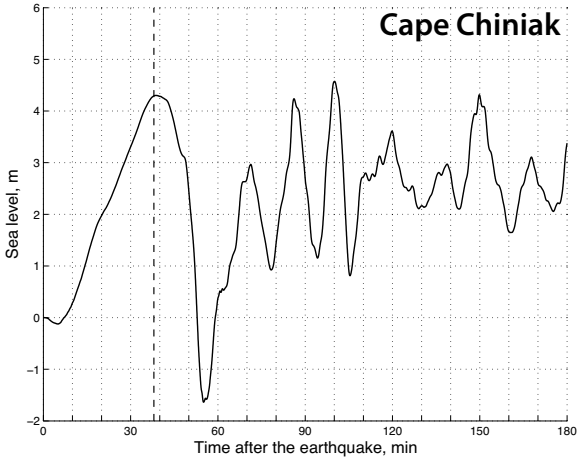
Cape Chiniak
Sea level, m
Time after the earthquake, min

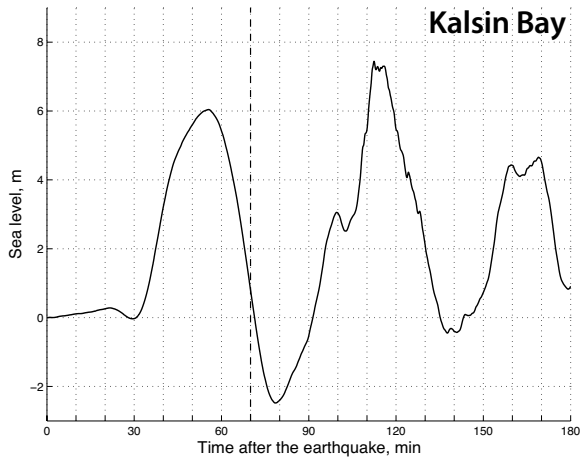
Kalsin Bay
Sea level, m
Time after the earthquake, min

Figure 14.

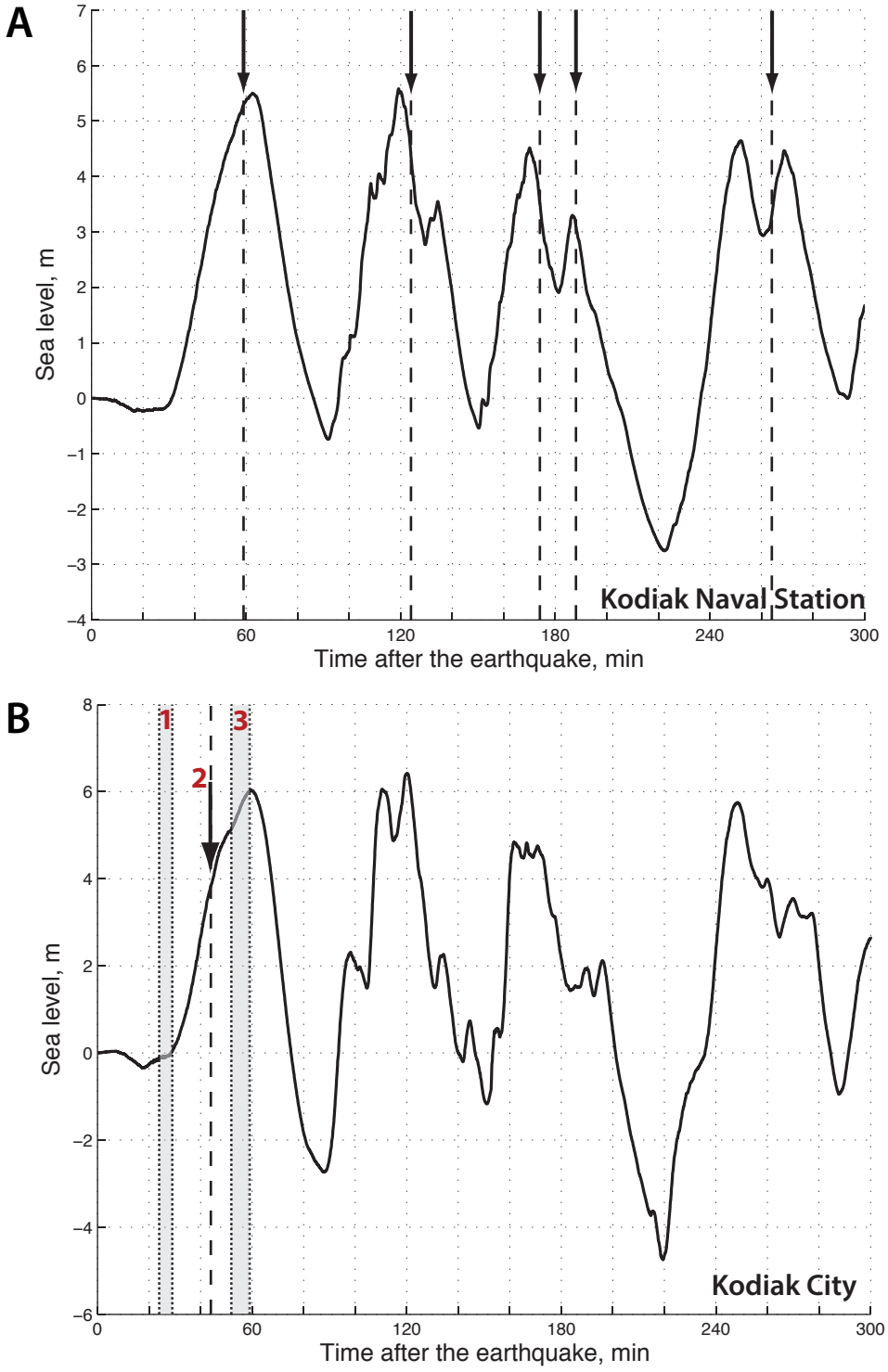
A
Sea level, m
Time after the earthquake, min
Kodiak Naval Station
B
1
2
3
Sea level, m
Time after the earthquake, min
Kodiak City